

# A Precise Measurement of the Deuteron Elastic Structure Function $A(Q^2)$

---

## INAUGURAL-DISSERTATION

zur Erlangung der Würde eines Doktors der Philosophie  
vorgelegt der Philosophisch-Naturwissenschaftlichen  
Fakultät der Universität Basel

von

Adrian Honegger-Feigenwinter

aus Rüti (ZH)

Basel 1999



Genehmigt von der Philosophisch-Naturwissenschaftlichen Fakultät  
auf Antrag der  
Herren Professor Dr. I. Sick und PD Dr. J. Jourdan.

Basel, den 7. Dezember 1999

Prof. Dr. S.M. Schmid  
Dekan



This work is dedicated to Nicole, Julian and my parents.

## Acknowledgements

I would like to thank my advisors Ingo Sick and Jürg Jourdan for their steady support and mentoring. Their doors were always open. I am very grateful for the given great deal of freedom and having had the possibility to participate in a vast number of experiments. Ingo is probably the most experienced electron–scatterer in the world. I have to admit that, concerning physics questions, he is almost always right! Jürg had to be one of the most patient advisors in the world, thank you very much JJ!

Furthermore, the  $T_{20}$  collaboration, lead by Betsy Beise and Serge Kox, deserves a special acknowledgement for having given David Pitz and me the possibility to extend the  $A(Q^2)$  measurements such that they became our thesis topic. I will never forget the sometimes (very) hot, always instructive, often encouraging and interesting discussions I had with numerous people of the collaboration.

Now, it's time to mention Rolfje LEnt, who helped and pushed me during my analysis year, and Beny, who saved my life when I tried to fry myself. They both became very close friends and Nicole and I will never forget that they showed up at our wedding.

My thesis is a result of the dedicated outstanding work of a lot of people at Jeffylab and in Hall C in particular. I would like to acknowledge all Hall C staff members, technicians and users I worked with. Allow me to do without a list, someone would for sure be forgotten.

My time at Jeffylab was a wonderful experience and I would not want to miss anything, not even the problems at the customs in Washington where it took the customer two hours to believe that the 27 kg of cheese were for personal use only!

The analysis was mainly done at the University of Basel. I am grateful to all members of the group for their technical, IT and moral support, to my Jeffylab mate Petit in special for his selfless cooperation and to the electronics workshop for their ideas and the “hotline” support during the installation of the cryo motor power supply. Furthermore I would like to thank David Pitz and his advisor Michel Garcon who were always valuable analysis partners.

## Abstract

During summer 1997 experiment e94-018 measured the deuteron tensor polarization in  $D(e, e'd)$  scattering in Hall C at Jefferson Laboratory. In a momentum transfer range between 0.66 and 1.8  $(\text{GeV}/c)^2$ , with slight changes in the experimental setup, the collaboration performed six precision measurements of the deuteron structure function  $A(Q^2)$  in elastic  $D(e, e'd)$  scattering. Scattered electrons and recoil deuterons were detected in coincidence in the High Momentum Spectrometer and the recoil polarimeter POLDER, respectively. At every kinematics  $H(e, e')$  data were taken to study systematic effects of the measurement. These new precise measurements resolve discrepancies between older data sets and put significant constraints on existing models of the deuteron electromagnetic structure.

This work was supported by the Swiss National Science Foundation, the French Centre National de la Recherche Scientifique and the Commissariat à l'Energie Atomique, the U.S. Department of Energy and the National Science Foundation and the K.C. Wong Foundation.

# Contents

<b>Abstract</b>	<b>i</b>
<b>Contents</b>	<b>ii</b>
<b>List of Figures</b>	<b>iv</b>
<b>List of Tables</b>	<b>vi</b>
<b>1 Introduction</b>	<b>1</b>
1.1 Deuteron Wave Functions . . . . .	1
1.2 Electron–Deuteron Elastic Scattering . . . . .	2
1.3 Motivation . . . . .	7
<b>2 Experiment</b>	<b>9</b>
2.1 Overview . . . . .	9
2.2 Accelerator . . . . .	9
2.3 Hall C Beamline . . . . .	10
2.3.1 Beam Position Measurement . . . . .	11
2.3.2 Beam Current Measurement . . . . .	11
2.3.3 Beam Rastering System . . . . .	14
2.3.4 Beam Energy Measurements . . . . .	14
2.3.5 Targets . . . . .	15
2.4 Electron Spectrometer . . . . .	18
2.5 Deuteron Spectrometer . . . . .	20
2.6 Data Acquisition . . . . .	22
<b>3 Extraction of the Differential Cross section</b>	<b>23</b>
3.1 Tracking Cuts . . . . .	23
3.2 Electron Identification Cuts and Background Rejection . . . . .	23
3.3 Selection of the e–d coincidences . . . . .	25
3.4 Electronic and Computer Dead Time . . . . .	26
3.5 Trigger Efficiency . . . . .	27
3.6 Tracking Efficiency . . . . .	27
3.6.1 Wrong $y'_{fp/tar}$ Selection . . . . .	29
3.7 Aluminum Target Window Subtraction . . . . .	31
3.8 Correction for finite acceptance and extended target . . . . .	32
3.9 Radiative Correction . . . . .	34
3.10 HMS/POLDER Acceptance Mismatch . . . . .	35
3.11 Deuteron (and Proton) Absorption . . . . .	37
3.11.1 Deuteron Loss occurring after the target . . . . .	38

3.11.2 Elastic d-d (p-p) Scattering in the Target . . . . .	38
3.12 Beam Angle and Offset . . . . .	39
3.13 Spectrometer Angle . . . . .	41
3.14 Systematic Uncertainties . . . . .	41
<b>4 Results and Discussion</b>	<b>42</b>
4.1 Electron-Proton Elastic Cross Sections . . . . .	42
4.2 Electron-Deuteron Elastic Cross Sections . . . . .	42
4.3 Extraction of $A(Q^2)$ . . . . .	43
4.4 Comparison with Theory . . . . .	47
4.4.1 Nonrelativistic Calculations . . . . .	47
4.4.2 Relativistic Calculations . . . . .	49
<b>5 Summary</b>	<b>49</b>
<b>A Electronic Dead Time</b>	<b>51</b>
<b>B Reduction of Kinematic Broadening</b>	<b>52</b>
<b>C Deuteron cross section calculations</b>	<b>53</b>
C.1 Theoretical Considerations . . . . .	53
C.2 Results of Deuteron Cross Section Calculations . . . . .	55
<b>Bibliography</b>	<b>60</b>

## List of Figures

1	Deuteron wave functions . . . . .	2
2	Structure functions $A(Q^2)$ and $B(Q^2)$ of the deuteron. . . . .	4
3	Tensor polarization $t_{20}$ of the deuteron. . . . .	4
4	Deuteron form factors $G_C(Q^2)$ , $G_M(Q^2)$ and $G_Q(Q^2)$ . . . . .	5
5	$A(Q^2)$ world data and theoretical models up to 1997. . . . .	7
6	Schematic view of accelerator and experimental halls. . . . .	10
7	Beam splitting and current adjustment for every hall. . . . .	10
8	Nb-cavity and its electric field distribution. . . . .	11
9	Schematic diagram of Hall C beamline. . . . .	12
10	Schematic of BPM. . . . .	13
11	Schematic of Superharp. . . . .	13
12	Schematic of Unser monitor. . . . .	13
13	Error in Arc dipole field integral. . . . .	15
14	Beam energy correction $\delta E/E$ . . . . .	15
15	Cryo target flow. . . . .	16
16	Boiling correction. . . . .	18
17	Side view of the HMS. . . . .	18
18	Dimensions of HMS collimator. . . . .	19
19	Side view of HMS detector stack. . . . .	20
20	HMS DC layout. . . . .	21
21	Schematic view of HMS scintillator array. . . . .	21
22	Top view of deuteron spectrometer. . . . .	21
23	Deuteron detection scintillators and MWPCs. . . . .	22
24	Pion and electron identification of inclusive runs. . . . .	24
25	Pion and electron identification of coincidence runs. . . . .	24
26	Raw TOF spectras of Kin I and VI. . . . .	25
27	TOF cut procedure. . . . .	25
28	Raw hadron ADC spectras of Kin I, V and VI. . . . .	26
29	Deuteron ADC cut finding procedure. . . . .	26
30	$\delta_{cor}$ distribution of kin I. . . . .	27
31	$\delta_{cor}$ distribution of kin VI. . . . .	27
32	Definition of fiducial area. . . . .	28
33	Deuteron cut for check of tracking efficiency. . . . .	28
34	Visualization of single electron track. . . . .	30
35	Visualization of tracking algorithm error. . . . .	31
36	$y'_{tar}$ distribution of run 15831. . . . .	32
37	$D(e,e'd)$ dummy subtraction. . . . .	33
38	$H(e,e')$ dummy subtraction. . . . .	33
39	Radiative corrections for $H(e,e')$ runs. . . . .	35

40	Radiative corrections for $D(e,e'd)$ runs. . . . .	35
41	Kin I deuteron distribution reconstructed at S2. . . . .	36
42	Kin VI deuteron distribution reconstructed at S1. . . . .	36
43	Picture of $H_2$ target exit window. . . . .	39
44	Invariant mass of $D(e,e'd)$ kin VI. . . . .	40
45	Relative ratios of invariant masses. . . . .	40
46	Electron-proton cross sections relative to a fit and models. . .	43
47	Electron-deuteron cross sections relative to a fit. . . . .	44
48	$A(Q^2)$ results relative to fit and models. . . . .	46
49	CEA background subtraction. . . . .	46
50	MEC Feynman graphs. . . . .	47
51	$A(Q^2)$ results compared to nonrelativistic model calculations..	48
52	$A(Q^2)$ results compared to relativistic model calculations. . .	50
53	$\delta$ versus $\theta$ distribution of kin VI. . . . .	52
54	$\delta_{cor}$ versus $\theta$ distribution of kin VI. . . . .	52

## List of Tables

1	Overview of D(e,e'd) kinematical setups. . . . .	9
2	Overview of Arc energies and corrections applied. . . . .	15
3	Scattering chamber window material. . . . .	16
4	Critical dimensions and quantities of cryo and dummy targets. . . . .	17
5	$D_2$ purity. . . . .	17
6	HMS performance overview. . . . .	20
7	Dimensions of deuteron detectors. . . . .	22
8	Deuteron detector efficiencies. . . . .	27
9	Tracking efficiency check. . . . .	29
10	Correction for finite acceptance and extended target. . . . .	33
11	Correction for finite acceptance and pointlike target. . . . .	33
12	Additional materials used for radiative corrections. . . . .	34
13	Radiative correction factors. . . . .	35
14	Simulated and measured mismatch corrections. . . . .	37
15	Materials used to calculate hadron losses. . . . .	37
16	Table of hadron losses in POLDER. . . . .	39
17	Analysis of Superharp scans. . . . .	40
18	Systematic uncertainties of $d\sigma/d\Omega$ . . . . .	41
19	Total systematic uncertainties. . . . .	41
20	Energy loss $E_{loss}$ in the target before interaction. . . . .	42
21	Electron-proton cross section results. . . . .	42
22	Electron-deuteron cross section results. . . . .	45
23	$A(Q^2)$ results. . . . .	45
24	D scattering, Serber model. . . . .	55
25	$^4\text{He}$ scattering, Serber model. . . . .	56
26	$^{12}\text{C}$ scattering, Serber model. . . . .	56
27	$^{14}\text{N}$ scattering, Serber model. . . . .	56
28	$^{16}\text{O}$ scattering, Serber model. . . . .	57
29	$^{27}\text{Al}$ scattering, Serber model. . . . .	57
30	H scattering, Glauber model. . . . .	57
31	D scattering, Glauber model. . . . .	58
32	$^4\text{He}$ scattering, Glauber model. . . . .	58
33	$^{12}\text{C}$ scattering, Glauber model. . . . .	58
34	$^{14}\text{N}$ scattering, Glauber model. . . . .	59
35	$^{16}\text{O}$ scattering, Glauber model. . . . .	59
36	$^{27}\text{Al}$ scattering, Glauber model. . . . .	59

# 1 Introduction

The six  $A(Q^2)$  measurements presented in this thesis were part of experiment e94-018, the *Measurement of the Deuteron Tensor Polarization* [2, 3], at Thomas Jefferson National Accelerator Facility (JLab). It was necessary to measure  $A(Q^2)$  to determine from the tensor polarization observable  $t_{20}$  the individual form factors. The experimental setup was modified such, that the collaboration was able to perform the  $A(Q^2)$  measurement with a systematic uncertainty of  $\sim 4\%$  and 1% statistical error.

The analysis of the elastic  $D(e,e'd)$  data and the extracted deuteron structure function  $A(Q^2)$  in a  $Q^2$  range between 0.66 and 1.8  $(\text{GeV}/c)^2$  provide a crucial test for any model of the deuteron.

## 1.1 Deuteron Wave Functions

An important goal of nuclear physics is to understand nuclear structure in terms of the underlying nucleon–nucleon (NN) interaction. The deuteron, as the smallest and simplest stable nucleus, is an ideal candidate for the investigation of our ability to calculate nuclear properties starting from the NN interaction. The attractive “long” ( $r \geq 2 \text{ fm}$ ) and “intermediate” ( $0.8 < r < 2 \text{ fm}$ ) range of the NN interaction are reasonably well described by boson exchange potentials, however the short–range repulsive part ( $r \leq 0.8 \text{ fm}$ ) is still poorly understood.

The deuteron’s ground state properties yield information about the character of the nuclear force. The nonrelativistic Schrödinger equation can be solved with a high degree of accuracy. Various modern potential models suggest a tensor force component in addition to the central potential. They all predict that the tensor force causes the deuteron to have a small admixture of a  $^3D_1$  state in addition to the dominant  $^3S_1$  state. Therefore, the deuteron wave function can be written as

$$\psi = R_0 Y_{110}^{M_d} + R_2 Y_{112}^{M_d} \quad (1)$$

with  $R_0 = u/r$  and  $R_2 = w/r$  the S– and D–state wave functions, respectively, normalized such that  $\int_0^\infty [u^2 + w^2] dr = 1$ , and  $Y_{JSL}^{M_d}$  the spin–angle functions. Characteristic shapes of the deuteron radial wave functions are shown in Fig. 1 for the Argonne V–18 potential model [4]. For  $r$  larger than the range of the interaction potential, the wave functions  $u(r)$  and  $w(r)$  are  $L = 0$  and  $L = 2$  exponentially decreasing “free wave” solutions corresponding to the binding energy  $E_B$ , with  $\alpha = \sqrt{\frac{1}{2} E_B (M_n + M_p)} = 0.23161 \text{ fm}^{-1}$ ,

$$u(r) \xrightarrow{r \rightarrow \infty} A_S e^{-\alpha r} \quad (2)$$

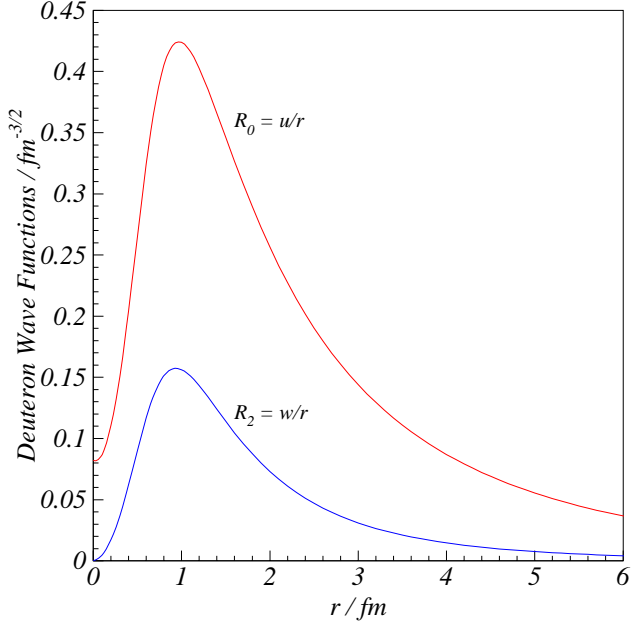


Figure 1: *Deuteron wave function components in configuration-space for the Argonne V-18 potential model [4].*

$$w(r) \xrightarrow{r \rightarrow \infty} A_D e^{-\alpha r} \left\{ 1 + \frac{3}{\alpha r} + \frac{3}{\alpha^2 r^2} \right\}. \quad (3)$$

The constants  $A_S$  and  $A_D$  are the asymptotic S- and D-wave amplitudes, which are normally given in terms of  $A_S$  and the asymptotic ratio  $\eta = A_D/A_S$ .

The presence of the repulsive core of the NN interaction is reflected by the sharp decrease of the S-state wave function at small  $r$ . This region is poorly understood due to lack of knowledge of the short range–range part of the NN interaction.

## 1.2 Electron–Deuteron Elastic Scattering

Various probes are used to investigate the internal structure of nuclei. Hadrons have the advantage of large cross sections because they interact strongly. The complication of the unknown nucleon structure and the reaction mechanism lead to difficulties in the interpretation of the results. When using an electromagnetic probe on the other hand, the interaction can be computed in the framework of quantum electrodynamics (QED).

In elastic electron-deuteron scattering, the energy of the scattered relativistic electron  $E_{e'}$  is given by

$$E_{e'} = f E_e. \quad (4)$$

$E_e$  is the incident electron energy and  $f$  the recoil factor

$$f = \frac{1}{1 + \frac{2E_e}{M_d} \sin^2 \frac{\theta_e}{2}}, \quad (5)$$

which takes into account the finite mass of the target nucleus.  $\theta_e$  and  $M_d$  are the electron scattering angle in the lab frame and the target mass, respectively. As energy and momentum of the scattering process are conserved, the four-momentum  $q = (\vec{q}, \omega)$ , carried by the virtual photon, can be expressed as a function of incident and scattered electron energy and the electron scattering angle:

$$Q^2 = \vec{q}^2 - \omega^2 = 4E_e E_{e'} \sin^2 \frac{\theta_e}{2} > 0. \quad (6)$$

The virtual photon is “space-like”. In the normal convention  $q_\mu^2$  is negative. For the sake of simplicity  $Q^2$  was introduced. It is related to the kinetic energy of the deuteron  $T_d$  via

$$T_d = E_e - E_{e'} = \frac{Q^2}{2M_d}. \quad (7)$$

In the one-photon-exchange or first Born approximation, the electron-deuteron unpolarized elastic differential cross section can be written as [5]

$$\frac{d\sigma}{d\Omega_e} = \left( \frac{d\sigma}{d\Omega} \right)_{\text{Mott}} f \left( A(Q^2) + B(Q^2) \tan^2 \frac{\theta_e}{2} \right), \quad (8)$$

where the Mott cross section describes the scattering of an electron off a pointlike spinless particle according to

$$\left( \frac{d\sigma}{d\Omega} \right)_{\text{Mott}} = \frac{\alpha^2 \cos^2 \frac{\theta_e}{2}}{4E_e^2 \sin^4 \frac{\theta_e}{2}}. \quad (9)$$

Here  $\alpha$  is the fine structure constant and  $c = \hbar = 1$ .

The longitudinal and the transverse structure function  $A(Q^2)$  and  $B(Q^2)$  (Fig. 2) are determined in cross section measurements. They can be expressed as combinations of the three Sachs form factors of the deuteron:

$$A(Q^2) = G_C^2(Q^2) + \frac{8}{9}\eta^2 G_Q^2(Q^2) + \frac{2}{3}\eta G_M^2(Q^2), \quad (10)$$

$$B(Q^2) = \frac{4}{3}\eta(1 + \eta)G_M^2(Q^2), \quad (11)$$

$$\text{with } \eta = \frac{Q^2}{4M_d^2}.$$

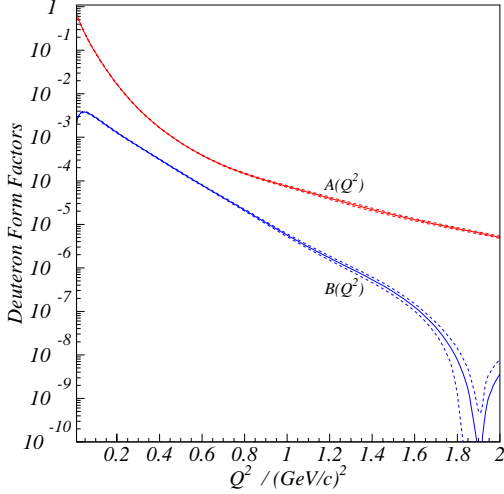


Figure 2: Structure functions  $A(Q^2)$  and  $B(Q^2)$  of the deuteron. Curves are a fit to world data.

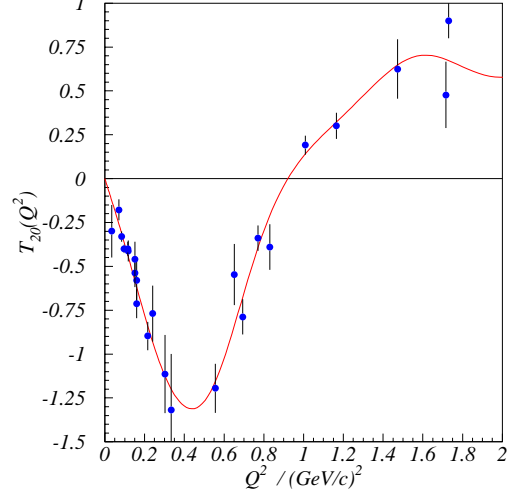


Figure 3: Tensor polarization  $t_{20}$  of the deuteron at  $70^\circ$ . Curve is a fit to the world data also plotted.

The structure functions  $A(Q^2)$  and  $B(Q^2)$  can be separated by varying the longitudinal polarization  $\epsilon$  of the virtual photon, given by

$$\epsilon = [1 + (2\vec{q}^2/Q^2) \tan^2 \frac{\theta_e}{2}]^{-1}, \quad (12)$$

between 0 and 1 while  $Q^2$  is kept fixed (Rosenbluth separation).

In order to separate the relative contributions of  $G_C(Q^2)$  and  $G_Q(Q^2)$  (Fig. 4) from  $A(Q^2)$ , a third observable has to be measured, e.g. the tensor polarization  $t_{kq}$  (Fig. 3) which describes the state of spin orientation of an assembly of particles. The general relations between the tensor polarization variables and the deuteron form factors are

$$t_{20} = -\frac{1}{\sqrt{2}I_0} \left[ \frac{8}{9}\eta G_C G_Q + \frac{8}{9}\eta^2 G_Q^2 + \frac{1}{3}\eta(1 + 2(1 + \eta) \tan^2 \frac{\theta_e}{2}) G_M^2 \right], \quad (13)$$

$$t_{21} = \frac{2}{\sqrt{3}I_0}\eta \left[ \eta + \eta^2 \sin^2 \frac{\theta_e}{2} \right]^{1/2} G_M G_Q \cos^{-1} \frac{\theta_e}{2} \quad \text{and} \quad (14)$$

$$t_{22} = -\frac{1}{2\sqrt{3}I_0}\eta G_M^2 \quad \text{with} \quad I_0 = A(Q^2) + B(Q^2) \tan^2 \frac{\theta_e}{2}. \quad (15)$$

While  $t_{20}$  shows a strong  $Q^2$  dependence,  $t_{21}$  and  $t_{22}$  are relatively  $Q^2$  independent and therefore of less importance for the separation of the form factors.

The normalization factors of the form factors (Fig. 4) are chosen such that at  $Q = 0$

$$G_C(0) = 1, \quad (16)$$

$$G_Q(0) = M_d^2 Q_d = 25.830, \quad (17)$$

$$G_M(0) = (M_d/M_p)\mu_d = 1.714 \quad \text{in units of } \mu_N, \quad (18)$$

with  $M_p$  the proton mass,  $Q_d = 0.28590(30) \text{ fm}^2$  the quadrupole moment,  $\mu_d$  the magnetic moment of the deuteron and  $\mu_N$  the nuclear magneton. The position of the node of  $G_C(Q^2)$  is very sensitive to various corrections such as meson exchange currents (MEC), relativistic effects, isobar currents (IC) and possible quark degrees of freedom (Sec. 4.4). High precision experimental data are necessary to study these effects and thus to probe the short range NN interaction.

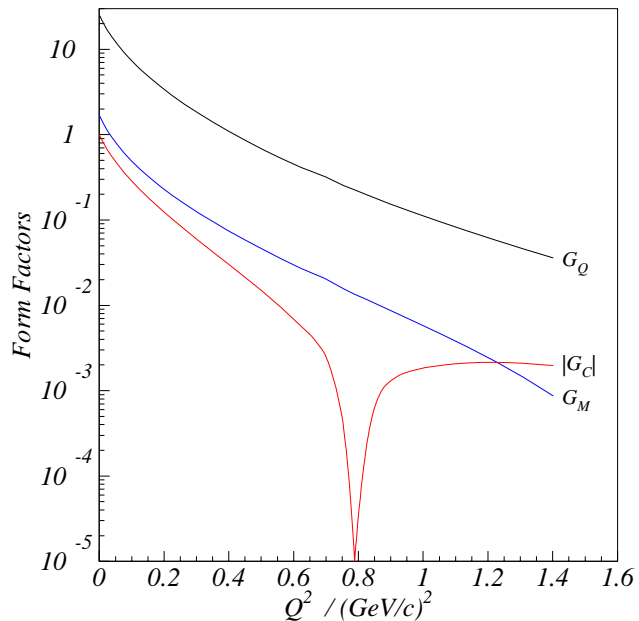


Figure 4: *Deuteron form factors  $G_C(Q^2)$ ,  $G_M(Q^2)$  and  $G_Q(Q^2)$ , based on NRIA calculation by B. Henning [6] using the PARIS potential, Simon proton and Galster neutron form factors.*

In elastic unpolarized e–d scattering, the recoil deuterons are tensor polarized. This experiment was part of a measurement of the tensor polarization  $t_{20}$ . The recoil deuterons were transported to a liquid hydrogen target, the recoil polarimeter POLDER [2, 7, 8], where they underwent the secondary  $^1H(\vec{d}, 2p)n$  reaction which allowed for the determination of the tensor polarization. The cross section for this secondary reaction is

$$\begin{aligned} \sigma(\theta, \phi) = & \sigma_0(\theta)[1 + 2it_{11}iT_{11}(\theta) + t_{20}T_{20}(\theta) \\ & + 2t_{21}T_{21}(\theta)\cos\phi + 2t_{22}T_{22}(\theta)\cos 2\phi] \end{aligned} \quad (19)$$

where  $t_{tk}$  are the polarization coefficients of the beam, in this case of the recoil deuterons, and  $T_{tk}$  the analyzing powers.  $\sigma_0$  is the cross section of the unpolarized beam and  $\phi$  the angle between the normal to the reaction plane and the spin axis of the incident particles. The analyzing powers  $T_{tk}$  and the unpolarized cross section  $\sigma_0$  were obtained in calibration experiments performed at the Laboratoire National SATURNE [2,9], France, having used  $\vec{d}$  beams with known intensity and polarization.

The theoretical understanding of the form factors will be discussed based on the nonrelativistic impulse approximation (NRIA) model. The main assumptions of the NRIA model are that the virtual photon interacts with the individual nucleons in the deuteron, and that the electromagnetic form factors of the nucleons in the deuteron can be described as the ones of free nucleons. The deuteron form factors  $G_C(Q^2)$ ,  $G_Q(Q^2)$  and  $G_M(Q^2)$  can be written in terms of the isoscalar nucleon form factors and the integral over the S- and D-state wave functions as

$$G_C = (G_E^p + G_E^n)C_E, \quad (20)$$

$$G_Q = (G_E^p + G_E^n)C_Q, \quad (21)$$

$$G_M = \frac{M_d}{M_p}((G_M^p + G_M^n)C_S + \frac{1}{2}(G_E^p + G_E^n)C_L), \quad (22)$$

where  $G_E^{p(n)}$  and  $G_M^{p(n)}$  are the electric and magnetic form factors of the proton (neutron), respectively. The deuteron structure is described by  $C_E$ ,  $C_Q$ ,  $C_L$  and  $C_S$  which can be calculated in good approximation from the non-relativistic deuteron wave functions  $u(r)$  and  $w(r)$ :

$$C_E = \int_0^\infty [u^2(r) + w^2(r)]j_0\left(\frac{Qr}{2}\right)dr, \quad (23)$$

$$C_Q = \frac{3}{\sqrt{2}\pi} \int_0^\infty w(r)[u(r) - \frac{w(r)}{2\sqrt{2}}]j_2\left(\frac{Qr}{2}\right)dr, \quad (24)$$

$$C_S = \int_0^\infty \{[u^2(r) - \frac{1}{2}w^2(r)]j_0\left(\frac{Qr}{2}\right) + \frac{1}{2}w(r)[\sqrt{2}u(r) + w(r)]j_2\left(\frac{Qr}{2}\right)\}dr, \quad (25)$$

$$C_L = \frac{3}{2} \int_0^\infty w^2(r)[j_0\left(\frac{Qr}{2}\right) + j_2\left(\frac{Qr}{2}\right)]dr, \quad (26)$$

with  $j_i$  the spherical Bessel functions.

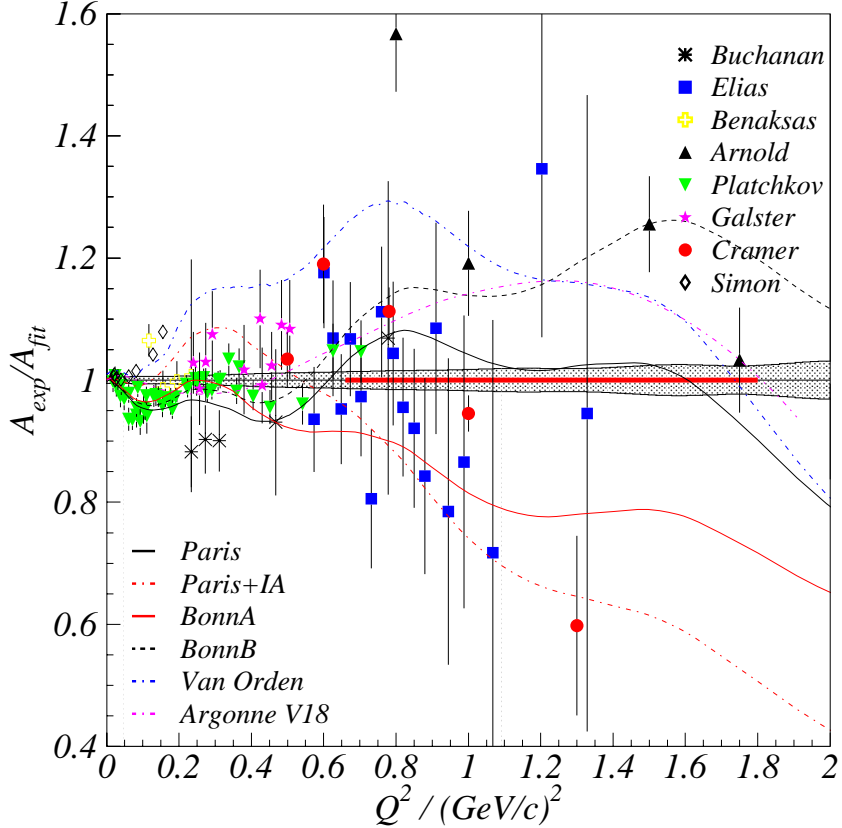


Figure 5:  $A(Q^2)$  deviations of [10–17] and selected models [18–21] from a world data fit. The red bar highlights the  $Q^2$  range covered by our measurements. The total error of the fit to the world data is shown by the hatched band.

### 1.3 Motivation

Figure 5, the ratio of the form factors to a fit, gives an overview of previous measurements of  $A(Q^2)$  which differ by as much as 40% from each other. They are going to be discussed in Sec. 4.3. The different models shown reproduce the data quite well, although with increasing  $Q^2$  deviations of up to 30% occur. The IA is successfully reproducing  $A(Q^2)$  up to  $Q^2 \simeq 0.3 (\text{GeV}/c)^2$ . Above, the predictions of many nonrelativistic models have to be augmented with corrections originating from meson-exchange currents (MEC) and relativistic contributions. The present treatment of MEC's is still incomplete and somewhat model dependent. Several relativistic treatments of the IA [22, 23] and more sophisticated models [24–26] have been published. A detailed discussion is given in [27].

In summary, the current situation is unsatisfactory. In addition to theoretical discrepancies among various models, there are inconsistencies between available data sets. Precise measurements are important in order to resolve the situation.

## 2 Experiment

### 2.1 Overview

The data analyzed in the present work were taken on isolated days during experiment e94-018 between April and September 1997. JLab provided continuous wave (CW) unpolarized electron beams with energies up to 4 GeV and currents of  $80 \mu\text{A}$  for  $D(e,e'd)$  runs and  $20 \mu\text{A}$  for  $H(e,e')$  calibration data. We used the High Momentum Spectrometer (HMS) to detect the scattered electron and the recoil polarimeter (POLDER) for the detection of the coincident deuteron or proton. The specific kinematics are summarized in Table 1.

Label	$Q^2$ ( $\text{GeV}/c^2$ ) <sup>2</sup>	$E_e$ GeV	$\theta_e$ deg	$\theta_d$ deg	$T_d$ MeV/nucleon
I	0.659	1.4118	35.82	60.5	86.7
II	0.787	1.6455	33.60	60.5	104.2
III	1.021	2.0980	29.93	60.5	134.9
IV	1.187	2.4464	27.63	60.5	156.7
V	1.516	3.2477	23.36	60.5	199.8
VI	1.797	4.0463	20.33	60.5	237.3

Table 1: *Kinematical setups of  $D(e,e'd)$ :  $\theta_e$  is the nominal HMS angle.*

### 2.2 Accelerator

JLab utilizes two superconducting radio frequency (RF) linear accelerators (LINACs), each 240 m long, combined with two recirculating arcs (Fig. 6). A thermionic gun delivered electrons leaving the cathode through a hole of 1 mm in diameter at an energy of 10 keV. They were then rastered with horizontal and vertical frequencies of 749 MHz and 499 MHz over a collimator with three holes, one for each hall (Fig. 7). After having split the continuous beam into consecutive beam bursts of  $\sim 1.67$  ps width, it is recombined and accelerated in 18 cavities to 45 MeV (corresponding to 400 MeV LINAC energy). Next the beam is injected into the LINAC with its  $2 \times 160$  Nb-cavities (Fig. 8) which are driven by clystrons at  $3 \times 499$  MHz = 1.497 GHz. In 1997 the electrons gained 400 MeV per LINAC. The two arcs consist of five (east) and four (west) separate lines, one for every path. The recirculated electron beam is placed on top of itself in each of the two LINACs.

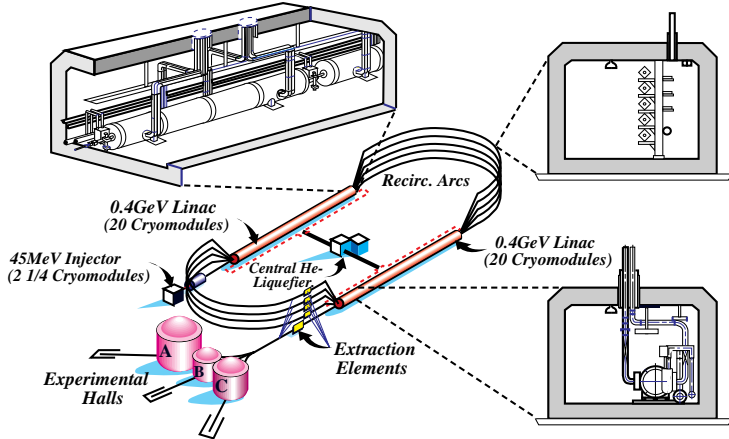
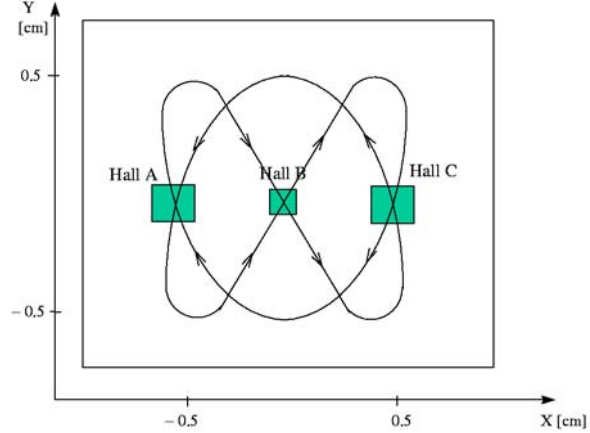


Figure 6: *Schematic view of accelerator and experimental halls.*

Figure 7: *After the thermionic gun, the beam is rastered with  $x$ - and  $y$ -frequencies of 749 MHz and 499 MHz over three holes. Its intensity can be adjusted for every hall by changing the area of the corresponding hole.*



The electron beam is not truly continuous. But as the dispersion of flight times in the spectrometer amounts to a few nanoseconds, the beam de facto has a quality that approaches the one of a CW beam. The energy dispersion of the beam  $\delta E/E$  is better than  $10^{-4}$  and the angular emittance is less than  $2 \times 10^{-9} \text{ m rad}$ .

### 2.3 Hall C Beamlime

After acceleration the electron beam is ejected from the south LINAC into the 42 m long Hall C arc which consists of eight identical dipoles, twelve quadrupoles, eight sextupoles, eight pairs of beam correctors, and several monitors measuring beam profile and position in order to determine the beam energy (Section 2.3.4). The Arc steers the beam to Hall C. The total deflec-

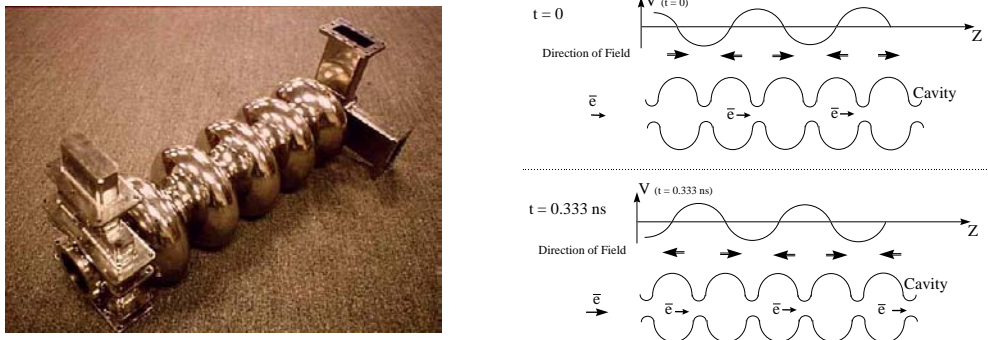


Figure 8: *Left:* Cavity with five cells. *Right:* Sine shaped potential and electric field at  $t = 0$  ns and  $t = 0.333$  ns.

tion angle is  $34.3^\circ$ . After the Arc, beam current (Section 2.3.2), profile and direction (Section 2.3.1) are monitored (Fig. 9).

### 2.3.1 Beam Position Measurement

The beam position monitor (BPM) is a non-intrusive device with a spatial resolution of 1.23 mm [28]. It consists of a cavity with four antennae located at  $\pm 45^\circ$  relative to the horizontal axis (Fig. 10). The intensity of the pick-up signal is proportional to the distance from the antenna to the beam. The position of the beam is determined from the ratio of the signals from opposing antennae. During our experiment BPM H00A did not work properly. The beam direction was therefore only monitored with Superharp scans.

The Superharp incorporates a tungsten wire which is moved through the beam by a stepper motor (Fig. 11) [29]. A shaft encoder reads the absolute position of the wire, and therefore of the beam, with an accuracy of  $\pm 200 \mu\text{m}$ . As the movement of the wire through the beam leads to a disruption of the latter, this device can not be used continuously.

### 2.3.2 Beam Current Measurement

The beam current measurement system [30–32] in Hall C consists of two different types of current monitors.

The **beam cavity monitor** (BCM) is a cylindrical wave guide. The beam passing through excites resonant modes that are picked up by wire loop antennae. The power in the antennae is proportional to the beam current squared. For certain modes the signal is insensitive to the beam position. The frequency of a mode depends on the size of the cavity which is chosen

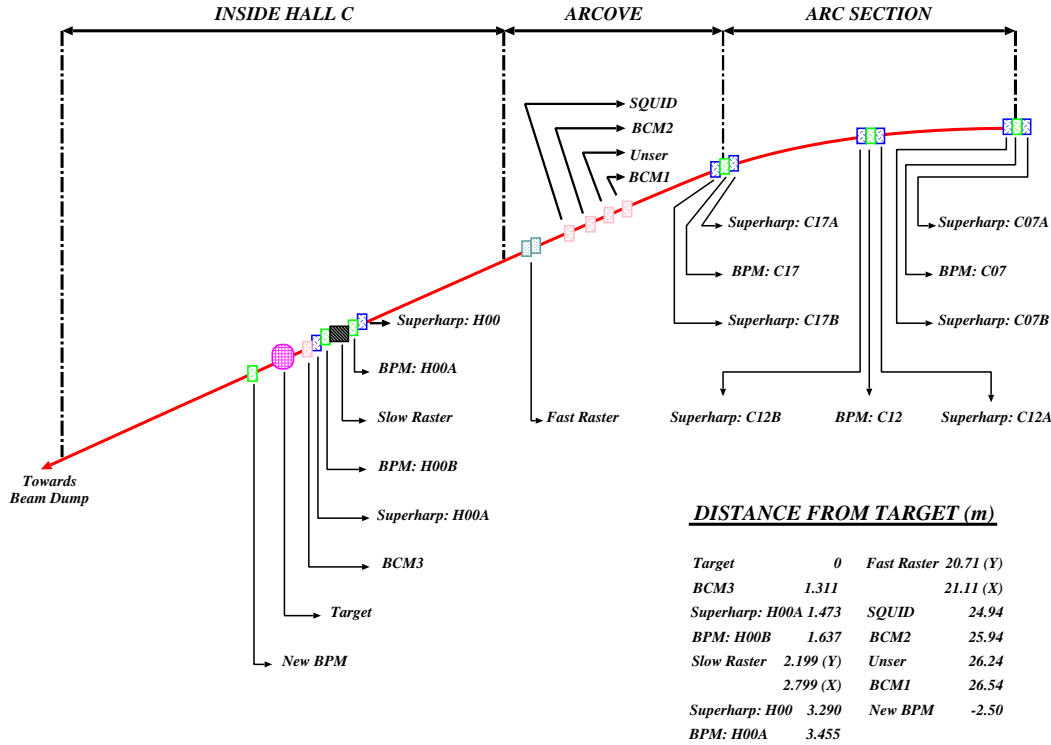


Figure 9: Schematic of Hall C beamline with major monitoring instrumentation shown.

such that the resonance frequency ( $f_{010}$ ) is identical to the RF frequency. As the measured quality factor  $Q = f_{010}W/P_d$ , the ratio of stored energy to dissipated weighted power, varies with material and length of the cavity, the BCM measurement shows a temperature dependence of  $\sim 0.25\%/\text{ }^\circ\text{C}$ . During e94-018 the temperature of the cavity was constantly monitored and stable within  $\pm 0.2\text{ }^\circ\text{C}$ . The uncertainty in the temperature of the readout electronics, located in the electronics room, also leads to an error of  $\sim 0.3\%/\text{ }^\circ\text{C}$ . As the temperature in the electronics room was stable to  $\pm 1\text{ }^\circ\text{C}$ , this introduced an uncertainty of  $\pm 0.3\%$ .

However, a cavity alone does not allow for an absolute current measurement as the power output depends on factors like surface finish which can not easily be quantified. It therefore needs to be calibrated.

The **parametric current transformer** (Unser monitor) [33–35] is used to calibrate the gain of the cavity. The Unser monitor has an extremely stable gain, but drifts in its offset ( $\sim 1\text{ }\mu\text{A}/24\text{ h}$ ). The monitor consists of two toroids and associated electronics. One of the toroids (Fig. 12) measures

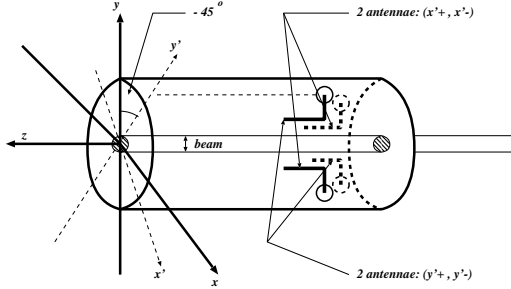


Figure 10: *Schematic of a BPM.*

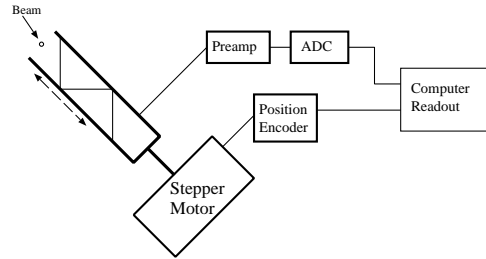


Figure 11: *Schematic of a Superharp.*

the AC, the other the DC currents. An AC modulator is used to drive the toroid along its hysteresis curve, which is symmetric in the absence of DC fluctuations. In the presence of the latter, however, the hysteresis curve is biased and loses its symmetry. A feedback loop restores the symmetry by delivering a DC current which is then measured. The gain of the Unser monitor was measured before, during and after the experiment. It was found to be stable to  $\pm 1.3 \times 10^{-4}$ .

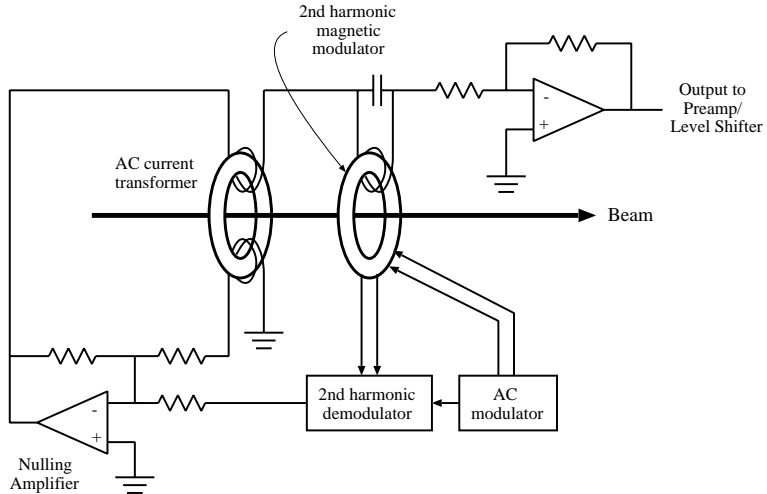


Figure 12: *Schematic of Unser monitor.*

BCM calibration runs were taken during every kinematical setup. The beam was alternately turned off, to measure both the offsets of both the Unser monitor and the BCMs, and to calibrate the gains of the BCMs using the known gain and the measured offset of the Unser monitor. The Unser monitor has an accuracy of  $0.2 \mu\text{A}$  which results in an uncertainty of 0.25% for  $D(e,e'd)$  runs (1% for  $H(e,e')$ ). Adding the temperature and the Unser uncertainty in quadrature, the overall uncertainty on the total charge is 0.4%

(1%).

### 2.3.3 Beam Rastering System

During experiment e94-018 only the fast raster (FR) was in operation. It is designed to prevent damage to the targets and reduce local boiling in the cryo targets. The FR magnets are located 25 m upstream of the target (Fig. 9). They are driven sinusoidally by 16 kHz in the vertical and 22.9 kHz in the horizontal direction. The raster size was set to  $\pm 1.0$  mm in both x and y during all  $A(Q^2)$  runs.

### 2.3.4 Beam Energy Measurements

The standard way to determine the beam energy is to measure the total field integral  $\int B dl$  required to bend the beam through the Hall C Arc (Fig. 9). Extensive studies using kinematic information [32,36,37] confirmed the Arc measurement and ensured its reliability. Due to the uncertainty of the beam direction of  $\pm 0.5$  mrad and its vertical position<sup>1</sup> of  $\pm 1.5$  mm (Table 17), a kinematic check of the beam energy measurement could not be performed with reasonably small errors.

After the experiment it was discovered that the cycling procedure for the Arc dipoles used during the experiment was different from the one used when the dipole fields were initially mapped. The energy measurements assumed a cycling up to  $I_{max} = 300$  A while in reality the dipoles were ramped up to  $I_{max} = 225$  A only. As a result the beam energy was overestimated (Fig. 13) and a correction ranging from 0.085 to 0.191%, depending on kinematics (Table 2) was applied. The correction has a relative uncertainty of 20% because the field as a function of the current is based on a single measurement, performed after the experiment was completed.

During the Arc measurement, which is not done continuously, all corrector magnets are turned off. Position and direction of the beam are measured at the beginning, middle and end of the Arc. With the precise knowledge of the  $\int B dl$  field integral and the absolute position of the beam, the beam energy can be determined with an uncertainty of  $\delta E/E \leq 1 \times 10^{-3}$ . This uncertainty is based on random variations of the beam energy measurements over the last five years [38]. During data taking the beam position in the middle of the Arc was constantly monitored and ensured to be stable within  $\pm 2$  mm. This position offset leads to an additional uncertainty of  $5 \times 10^{-4}$ .

---

<sup>1</sup>A 1 mm vertical beam offset at the pivot results in a 0.08% dispersion and thus momentum offset at the focal plane of HMS.

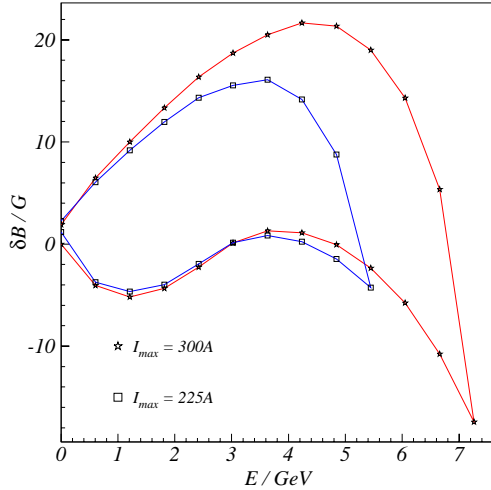


Figure 13: Deviation from linear relation between beam energy  $E$  and magnetic field  $B$  of an Arc dipole magnet as a function of  $I_{max}$ .

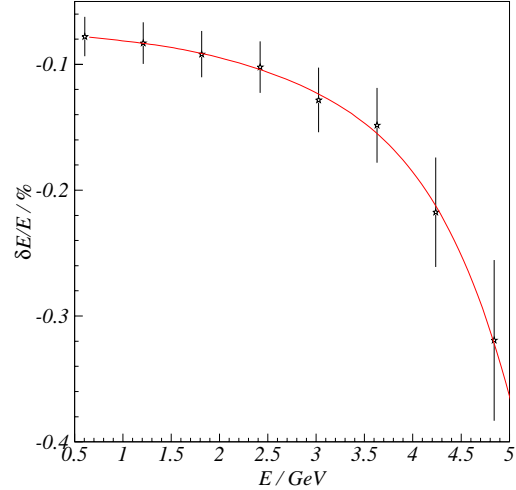


Figure 14: Correction applied to the beam energy measured by the Arc. It has an uncertainty of 20%.

Adding the uncertainties in quadrature, the beam energy uncertainty becomes  $1.2 \times 10^{-3}$ .

### 2.3.5 Targets

Both cryo and solid targets were accommodated in an aluminum scattering chamber of 123 cm diameter. Window materials used are listed in Table 3.

For the  $A(Q^2)$  experiment we only used the short hydrogen and deuterium cryo cells and the dummy target. Fig. 15 gives an overview of the cryo cells

Label	$E_{Arc}$ / GeV	$\delta E/E$ / %	$E_{Arc}^{Corr}$ / GeV
I	1.4130	-0.085	1.4118
0, II	1.6470	-0.088	1.6455
III	2.1000	-0.096	2.0980
IV	2.4490	-0.105	2.4464
V	3.2520	-0.133	3.2477
VI	4.0540	-0.191	4.0463

Table 2: Overview of the beam energy correction due to an incorrect cycling procedure. The absolute error on the corrected beam energy is 0.12%. At kin 0, only  $H(e, e'p)$  coincidence data were taken.

Window / mm	D( $e, e'd$ ) HMS + POLDER	H( $e, e'(p)$ ) HMS	H( $e, e'(p)$ ) POLDER
0.1524 Kevlar, 0.0381 Mylar	I - V <sub>16/06/97</sub>	I - IV	N/A
0.2032 Al	V <sub>26/06/97</sub> - VI	V - VI	0

Table 3: *List of scattering chamber window materials used. On June 16th, due to radiation damage, the scattering chamber window towards POLDER started leaking. All chamber windows were replaced. H( $e, e'p$ ) coincidence data were taken at kinematics O, all other hydrogen data come from single arm measurements.*

used. Table 4 lists crucial dimensions and offsets for each target [39,40].

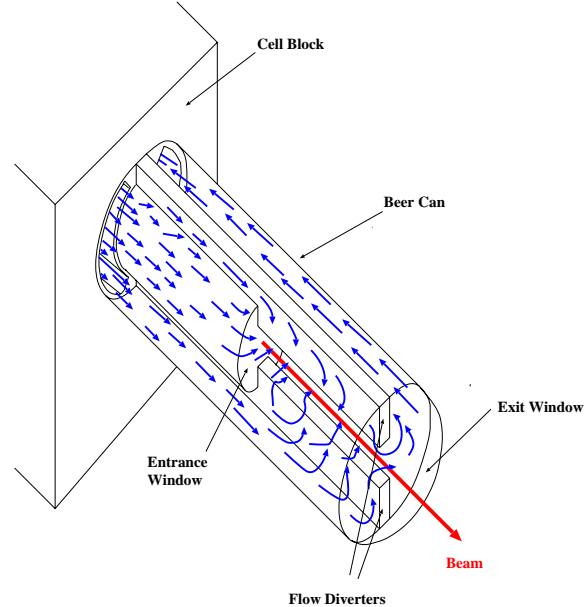


Figure 15: *Schematic view of  $D_2$  and  $H_2$  target cell. The flow diverters have the purpose of reducing local boiling by inducing turbulent flow.*

Since the cell exit windows were convex, the beam position and its direction at the target affected the effective target length. Having had a sinusoidal 1mm amplitude fast raster, a  $(2.6 \pm 0.6)$  mm radial and a  $(1.4 \pm 0.3)$  mrad angular offset, the effective target length for both cryo targets was only decreased by 0.03%. Angular and radial beam offsets at the target are described in more detail in Section 3.12. No correction was applied.

To estimate the effect of localized boiling in the target, D( $e, e'$ ) and H( $e, e'$ ) data were analyzed with suitable electron identification and tracking parameters selected. By examining the dependence of the normalized yield on beam current we estimated the localized boiling in the target (Fig. 16) to decrease the deuterium density by  $(1.7 \pm 0.5)\%$  when running with a beam current of

	D <sub>2</sub>	H <sub>2</sub>	Dummy
Cold Length / cm	4.45±0.01	4.53±0.01	4.00±0.04
Entr. Win. / cm	0.0071±0.0003	0.0071±0.0003	0.0960±0.0003
Exit Win. / cm	0.0114±0.0005	0.0104±0.0005	0.0967±0.0003
Side Walls / cm	0.013±0.005	0.013±0.005	N/A
Width / cm	6.73±0.08	6.73±0.08	N/A
Density / g/cm <sup>3</sup>	0.1670±0.0013 (T=22K, p=1.379bar)	0.07230±0.0005 (T=19K, p=1.655bar)	27.199±0.004 27.697±0.005
x Offset / cm	0.00±0.02	-0.13±0.02	N/A
y Offset / cm	-0.02±0.02	-0.04±0.02	N/A
z Offset / cm	-0.1±0.03	0.06±0.03	N/A

Table 4: *Critical dimensions and quantities of cryo and dummy targets. For the entrance window, Al5052 was used (Exit window: Al3003). The survey coordinate system is assumed, which means +x for beam left, +y for beam up, +z along the beam.*

80  $\mu$ A and a raster amplitude of  $\pm 1$  mm. For the hydrogen target, where we ran at 20  $\mu$ A only and no correction was applied.

Chemical gas analyses were performed before and after the experiment. The purity of the hydrogen gas was always found to be higher than 99.8% where the largest contaminations were nitrogen and oxygen which are both frozen onto the surface of the heat exchanger at the operating temperature of 19 K. Thus the contamination in the target cell is negligible. No correction is applied.

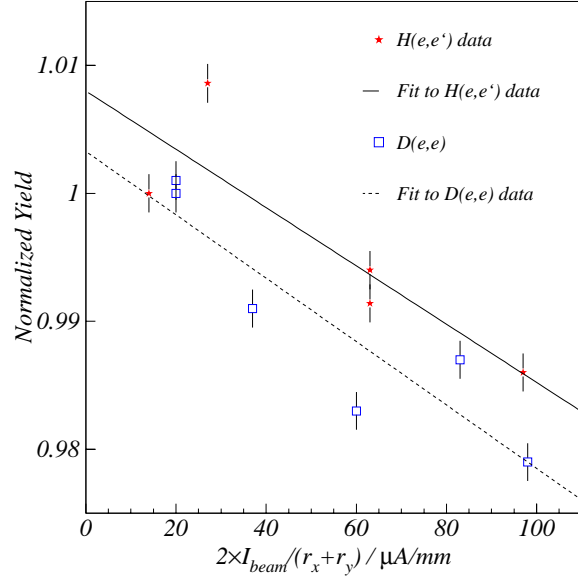
In contrast to the hydrogen loop, the deuterium loop had to be topped off

Label	I	II	III	IV	V	VI
Purity / %	98.71	98.81	98.71	98.60	98.52	98.41

Table 5: *Deuterium purities in view of the fact of the increasing hydrogen contamination. Kin II was measured first. The absolute uncertainty of the D<sub>2</sub> purity is 0.3%.*

by roughly 0.14 bar every month. Unfortunately, the refill bottle was contaminated with 2.03% hydrogen and 0.47% deuterium hydride. Although hydrogen has not liquefied at 22 K and 1.38 bar, the solubility of hydrogen gas in liquid deuterium was estimated [42] to be close to 100%, e.g. a 2% hydrogen contamination in the gas phase leads to a 2% hydrogen impurity at 22 K and 1.38 bar. Logbook records allowed us to determine the top-off dates as well as the amount of gas added. The steplike decrease of the deu-

Figure 16: *Local boiling data taken in April 97. The yield was found to scale with the ratio between the beam current  $I_{beam}$  and the mean raster amplitude  $(r_x + r_y)/2$  [41].*



terium purity could only be determined inaccurately with a systematic error of  $\sim 25\%$  leading to a total systematic uncertainty of the deuterium purity of  $0.3\%$ . Table 5 lists the estimated deuterium purities used in the analysis. Kinematics II was measured first. Due to uncertainties in temperature ( $0.5\%$ ), localized boiling ( $0.5\%$ ) and deuterium purity ( $0.3\%$ ), an overall uncertainty of  $0.8\%$  ( $0.7\%$  for  $\text{H}_2$ ) was applied to the final calculation of the effective target length.

## 2.4 Electron Spectrometer

The electrons were detected in the QQQD High Momentum Spectrometer (HMS) (Fig. 17), operated in a point-to-point tune.

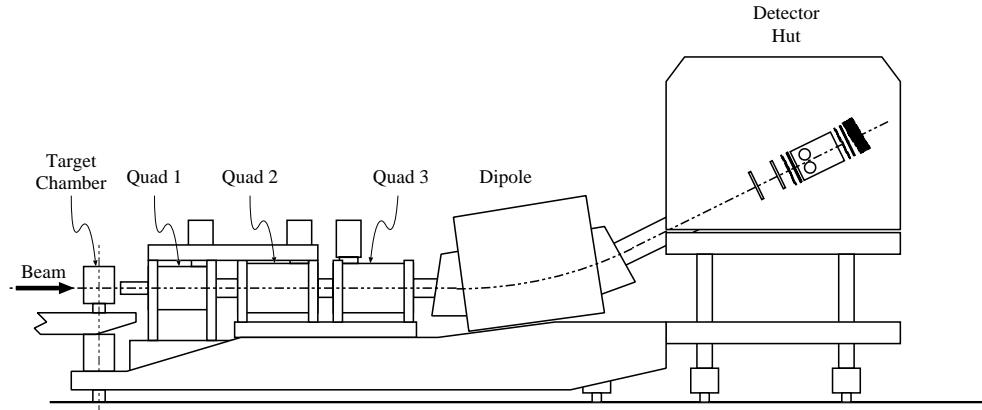


Figure 17: *Side view of the HMS.*

The magnetic field of the dipole was regulated using NMR probes located in a region of uniform field. The quadrupoles were set to the desired strength by choosing the appropriate current.

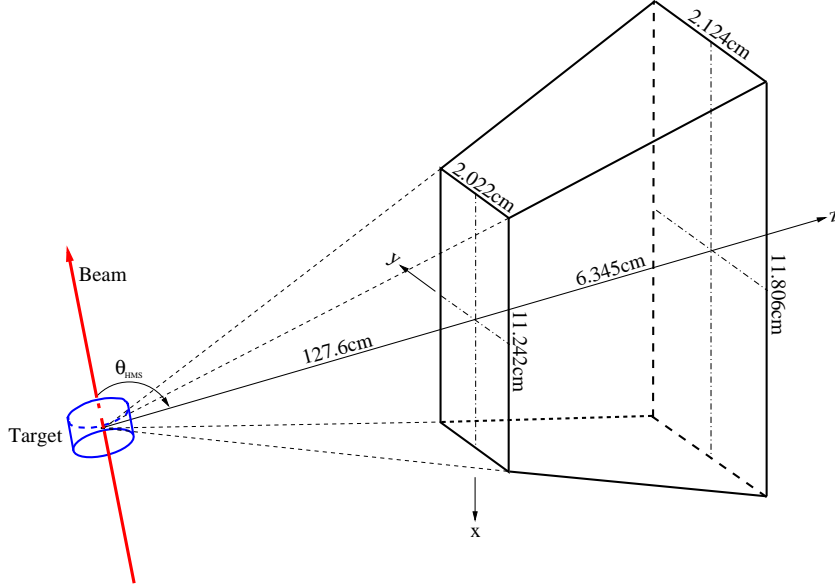


Figure 18: *Schematic view of the HMS collimator.*

The angular acceptance of the experiment was defined by a rectangular tungsten collimator located in a movable slit, placed in front of the HMS at a distance of 127.6 cm from the beam-target interaction point (Fig. 18). The design of the experiment was such that the phase space of the deuteron spectrometer covered both the angular and the momentum acceptance of the HMS. At the same time, the HMS collimator was chosen such as to guarantee that all electrons passing the collimator would (if they had the right energy) reach the focal plane detectors. Thus the solid angle of the experiment (Sec. 3.8) was simply given by the dimensions of the HMS collimator. No Monte Carlo simulation was needed.

The HMS is equipped with two drift chambers, two pairs of scintillator arrays, a threshold gas Čerenkov detector and a lead glass electromagnetic calorimeter (Fig. 19).

- The **HMS drift chambers** (DCs) provide track information. Both consist of six planes of sense wires (Fig. 20). They cover an active area of 113 cm vertical and 52 cm horizontal, respectively.
- The scintillator arrays generate the trigger for the electronics. Each pair consists of 16 scintillators arranged in the horizontal and 10 in

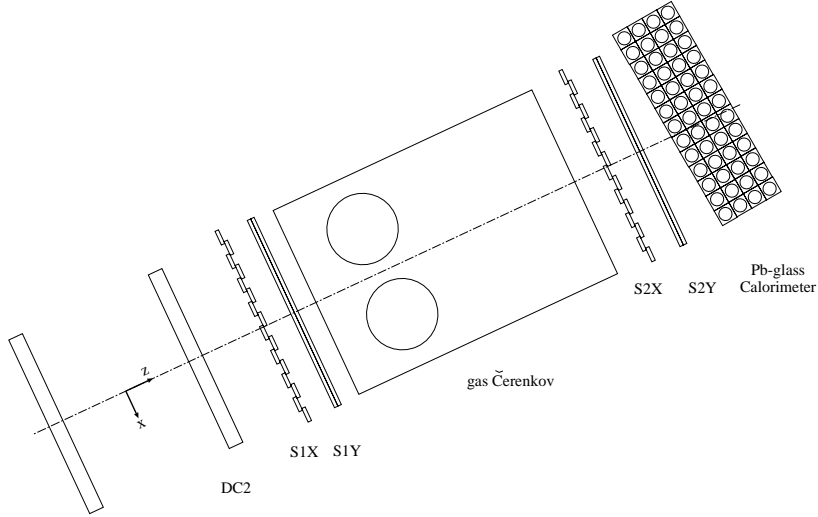


Figure 19: *Side*<sup>DC1</sup> view of the HMS detector stack. The scattered electrons pass from left to right.

the vertical direction, 75.5 cm and 120.5 cm long, respectively. All are 1 cm thick and 8 cm wide overlapping on each side by 0.5 cm with their neighbours.

The electron trigger [32, 43] was provided by a coincidence between 3 out of 4 scintillator plane signals (Fig. 21). A “good” hit in a plane was defined as a coincidence between at least one signal from a positive and a negative end of any bar of this plane.

- Both Čerenkov detector and Pb glass calorimeter are used to reject pions. The current experiment used only the Pb glass calorimeter for reasons explained in Section 3.1.

Momentum Resolution $\delta p/p$	0.1%
Angular Reconstruction (in plane)	$\pm 1$ mrad
Angular Reconstruction (out of plane)	$\pm 1$ mrad

Table 6: *Summary of important HMS performances* [44].

Further information on design, calibration and performance of the various detector elements can be found elsewhere [32, 36, 37, 43, 45, 46].

## 2.5 Deuteron Spectrometer

The purpose of the  $Q_1 Q_2 S Q_3 D$  deuteron spectrometer (Fig. 22) [2, 47] was to transport the deuterons to the secondary  $H_2$  target, where, via  $H(\vec{d}, 2p)n$

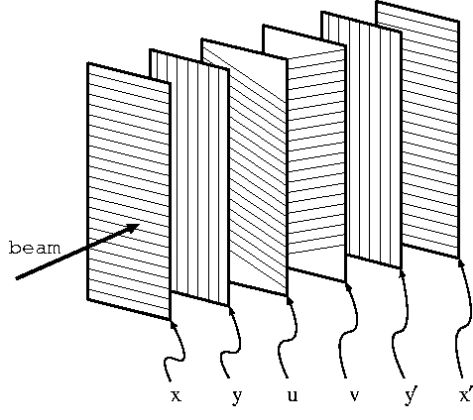


Figure 20: *Schematic diagram of DC layout.*

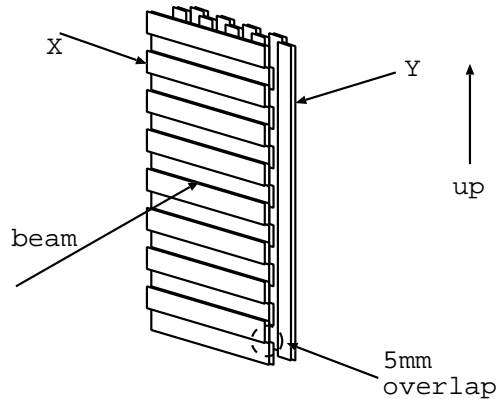


Figure 21: *Schematic diagram of a pair of scintillator arrays.*

charge exchange, the tensor polarization of the deuterons was measured using the *POLarimètre à DEuton de Recul* (POLDER) [2, 7, 8]. The deuteron arm was fixed at  $60.5^\circ$ . It had an out-of-plane (in-plane) angular acceptance of  $\pm 130$  mrad ( $\pm 80$  mrad) and a momentum acceptance which completely overlapped the HMS momentum acceptance. In order to reduce multiple scattering the transport channel was filled with a 775 cm long helium bag.

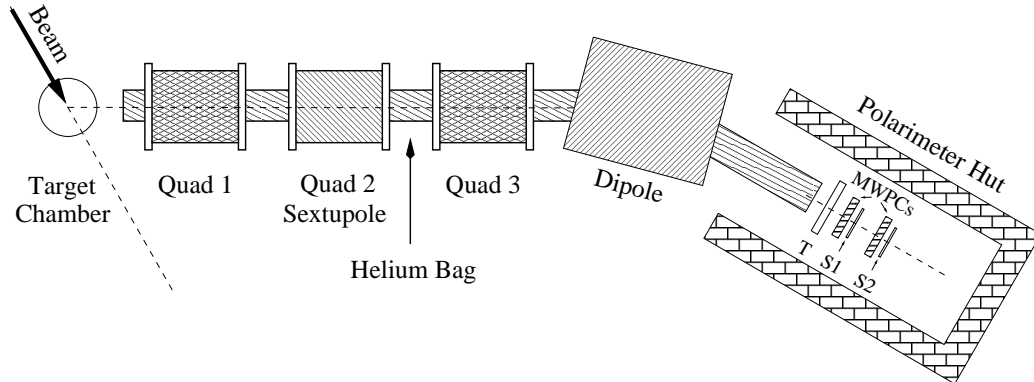
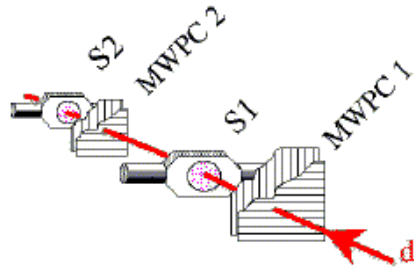


Figure 22: *Schematic top view of deuteron spectrometer. In the polarimeter hut, only the scintillators and MWPCs used for  $A(Q^2)$  are plotted.*

For kinematics I-III, a coincidence between the scintillators S1 and S2, both read out on two sides, started the time-of-flight (TOF) TDC, stopped by the corresponding electron triggering the coincidence. For kinematics IV-VI, only S1 was in the trigger. Large sliding scintillators T1 & T2, located in front of the whole detection apparatus (Fig. 23, Table 7) were mainly

Figure 23: *Schematic view of deuteron detection setup.*



used during the optimization procedure after a kinematics change. They were moved into the hadron beam during kinematics VI in order to measure the acceptance mismatch between the two spectrometers (Sec. 3.10) and the intrinsic hadron detection efficiencies of the S1 and S2 scintillators (Sec. 3.5).

The analog signals of the detectors permitted additional discrimination between deuterons and background protons of the same momentum. Two multiwire proportional chambers (MWPCs) allowed a determination of the deuteron (and proton) distribution. More details can be found in [2].

	Active Area cm <sup>2</sup>	Thickness mm	Distance to S1 cm	TOF trigger
S1	$20.0 \pm 15.0$	1.00	0	I-III
S2	circular, 144.0	2.00	46.6	I-IV
T1/2	$20.3 \pm 61.0$	6.35	102.8	VI

Table 7: *Dimensions of deuteron detectors. Trigger: Kin I-III, S1 and S2 in coincidence; kin IV-VI, S1 only; kin VI (run 15832) T1+T2 only.*

## 2.6 Data Acquisition

Physics data acquisition at JLab was accomplished with the CEBAF Online Data Acquisition (CODA) routines [48]. They ran on and controlled a network of front end controllers, known as Readout Controllers (ROCs). In addition to the data from the spectrometers, information from beamline sources, scalers and various databases were collected into the data stream. For further information the interested reader is referred to [2, 32, 36, 43].

### 3 Extraction of the Differential Cross section

We have measured the elastic differential  $D(e,e'd)$  cross section at six momentum transfers. To study the systematic effects of the experiment, six inclusive  $H(e,e')$  and one exclusive  $H(e,e'p)$  differential cross section measurements were also performed.

A differential cross section is defined as the probability of a projectile with energy  $E$  to interact with a target and to be detected in a solid angle element  $d\Omega$  at a certain angle  $\theta$ . It can be written as

$$\frac{d\sigma}{d\Omega_e}(E, \theta) = \frac{\text{number of good coincidences}}{\Omega_e \cdot \underbrace{n_e \cdot n_d}_{\mathcal{L}} \cdot \varepsilon}, \quad (27)$$

with  $\mathcal{L}$  the luminosity and  $\varepsilon$  the total efficiency (trigger, tracking, radiative corrections, mismatch, deuteron loss, dead time, finite acceptance correction).

Sections 3.1 through 3.12 discuss the inputs of Eqn. 27. Only non-standard experiment specific procedures are going to be discussed. The interested reader is referred to [32, 36, 37, 43] where the HMS is described in extensive detail.

#### 3.1 Tracking Cuts

The event reconstruction of the HMS generated focal plane ( $x_{fp}$ ,  $y_{fp}$ ,  $x'_{fp}$  and  $y'_{fp}$  with  $\hat{z}$  parallel to central ray,  $\hat{x}$  downwards and  $\hat{y}$  left) and target quantities ( $\delta = (p_{recon} - p_0)/p_0$  with  $p_0$  and  $p_{recon}$  the central and the reconstructed momentum respectively of HMS;  $y_{tar}$  the horizontal position at the target;  $x'_{tar}$  and  $y'_{tar}$  the tangents of the out-of- and in-plane scattering angles).

Due to the fact that the present experiment used the short (Table 4) targets and a small collimator (Fig. 18), the scattered electrons only illuminated the central 30% of the HMS acceptance. In the final analysis, no cuts on reconstructed quantities other than a cut on  $\delta$  were used.

There are no reconstructed quantities on the hadron side.

#### 3.2 Electron Identification Cuts and Background Rejection

In addition to electrons, the HMS detected mostly pions having the same momenta. They were rejected by requiring the detected particle to have an energy fraction  $E_{cal}/p$  greater than 0.6 deposited in the calorimeter.  $E_{cal}$  is

the electron energy, measured by the calorimeter. For the inclusive hydrogen runs, this cut was rejecting pions only between 68% and 95% (1– $2\sigma$  level for a pion energy resolution of  $\Delta E/E = 0.45/\sqrt{E(\text{GeV})}$ ) [49, 50]. However, as the  $\pi/e$  ratio was smaller than  $10^{-3}$  for these runs, a calorimeter cut rejected all pions (Fig. 24). For all coincidence runs, the  $\pi/e$  ratio was smaller than  $10^{-4}$  and a calorimeter cut would not have been necessary (Fig. 25).

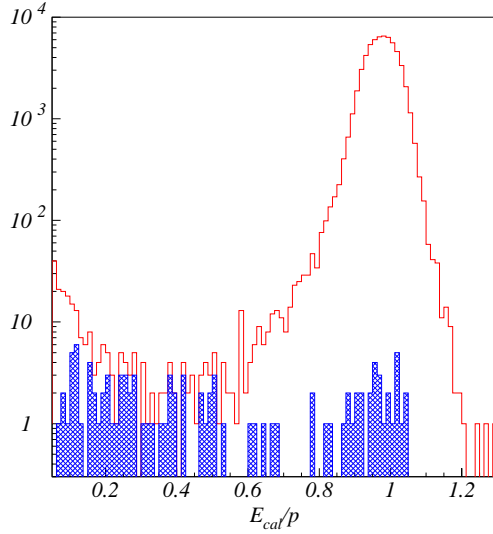


Figure 24:  $H(e, e')$  run 15837: Energy fraction deposited in the calorimeter. A  $\delta$  cut has been applied to both curves. Red:  $e$  and  $\pi$ . Blue hatched: after additional Čerenkov cut ( $\leq 1$  photo electron).

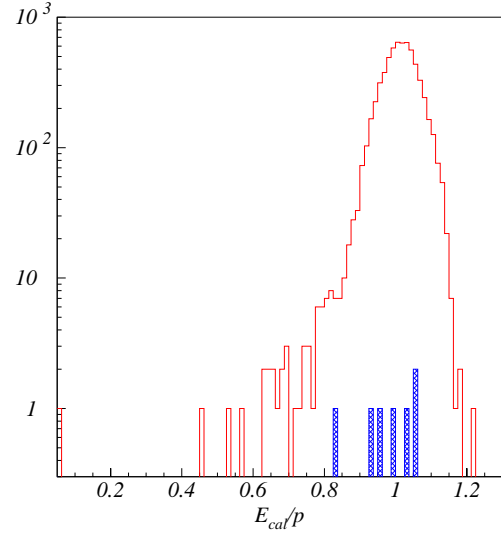


Figure 25:  $D(e, e'd)$  run 14628: Energy fraction deposited in the calorimeter. A  $\delta$  and a coincidence cut have been applied to both curves. Red:  $e$  and  $\pi$ . Blue hatched: after additional Čerenkov cut ( $\leq 1$  photo electron).

No cut on the Čerenkov signal was applied as the analysis showed that the electron detection inefficiency, the probability to misidentify an electron as a pion, was larger than the  $\pi/e$  ratio. Figure 24 shows a calorimeter spectrum of inclusive particles (a 4%  $\delta$  cut has been applied to both curves.). While the red curve represents pions as well as electrons, the blue hatched distribution only shows particles which have no or a single photo electron in the Čerenkov counter. We clearly see the peak to the right which represents the missed electrons (0.058%). The rare events to the left are pions (0.038%). Figure 25 shows the same plot for  $D(e, e'd)$  data. Having applied a coincidence timing cut in addition to the  $\delta$  cut, all pions could clearly be rejected without a calorimeter cut.

### 3.3 Selection of the e-d coincidences

To discriminate e-d from quasielastic e-p coincidences, we applied

- a time-of-flight (TOF) cut. The hadron starts the TDC which is stopped by the coinciding electron. The TOF difference between ed and ep coincidences varied between 30ns at kin I and 13ns at kin VI (Fig. 26). The TOF cuts were determined by looking at the derivative

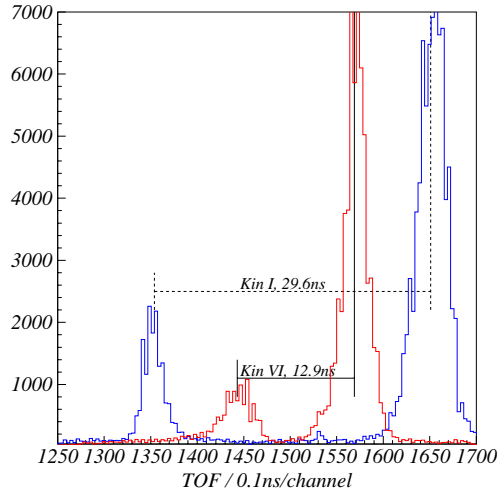


Figure 26: Raw TOF spectras of kin I and VI.

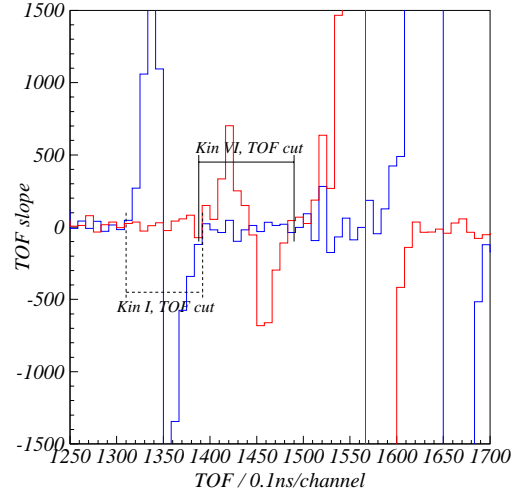


Figure 27: TOF derivatives (Forward difference between each bin of the raw TOF spectras) as a function of the TOF.

of the TOF distribution (Fig. 27). Accidental were subtracted applying a TOF cut on either side of the e-d peak, each cut having half the width of the main TOF cut.

- a dE/dx energy loss (or ADC) cut on the S2, S1 or T1+T2 (for run 15832) scintillator signals of POLDER (Fig. 28). The ADC cut was optimized by looking for a decrease in the number of e-d coincidences in the TOF peak while increasing the ADC cut (Fig. 29).
- an electron momentum cut in order to discriminate the quasielastic e-p coincidences. Fig. 30 and 31 show that a TOF and a dE/dx cut alone did not eliminate all e-p coincidences. In case of kin VI, we see that the smallness of the pathlength differences between *slow* protons and *fast* deuterons were leading to a slight ep contamination in the ed TOF

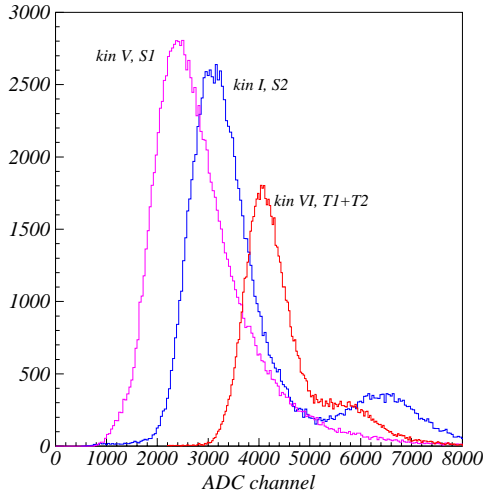


Figure 28: Raw ADC spectra of kin V, I and VI.

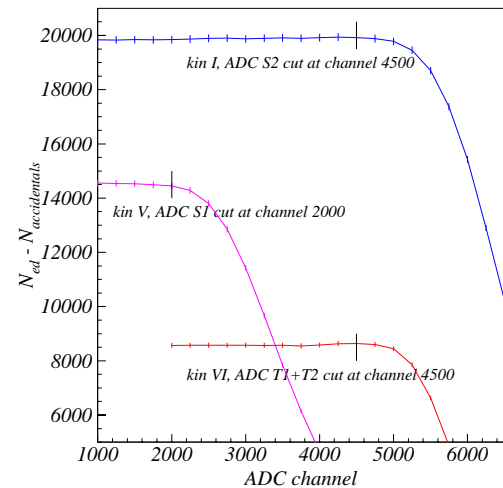


Figure 29: Number of remaining ed coincidences as a function of the ADC cut, no  $\delta$  cut was applied.

peak. The finite angular acceptance of the spectrometer and the angular dependence of the scattered electron momentum had been corrected for by Taylor-expanding the momentum of the scattered electron  $p(\theta)$  around  $\theta_{HMS}$  leading to  $\delta_{cor}$  (App. B). A momentum cut at  $-4\%$  was applied to all runs (Section 3.9).

### 3.4 Electronic and Computer Dead Time

There are two types of dead time. First the electronic dead time which results from events missed because the logic modules are busy processing previous events. During  $A(Q^2)$  data taking the electronics deadtime was always less than 0.5%. Its determination is discussed in more detail in Appendix A.

The second type is the computer dead time. It is due to the busy state of the data acquisition system caused by “slow” data transfer over the network. The computer dead time is simply given by the relation  $1 - (\text{pretrigger}/\text{trigger})$  where the trigger and pretrigger rates were measured using “deadtime-free” scalers. This correction was in the range of 0.5% to 7.8% for the coincidence runs with acquisition rates between 6 and 97 Hz and between 7.9% and 20.2% for the inclusive  $H(e,e')$  measurements. By varying the prescale factors, a study of the computer dead time was performed. The effective number of events per unit charge after applying the dead time correction was constant within 0.2% [51]. Therefore, the systematic uncertainty for all runs is 0.2%.

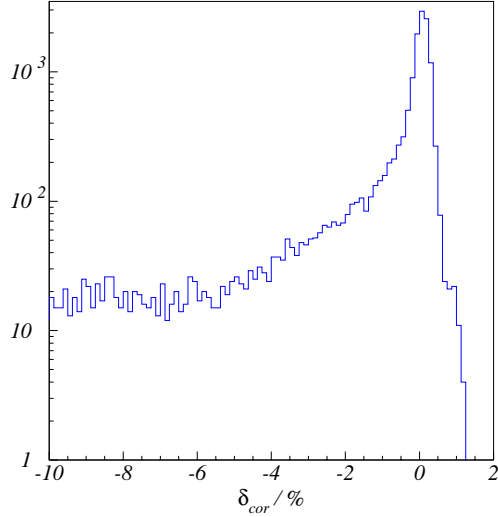


Figure 30:  $\delta_{cor}$  distribution of kin I. Calorimeter, TOF and  $dE/dx$  cut have been applied.

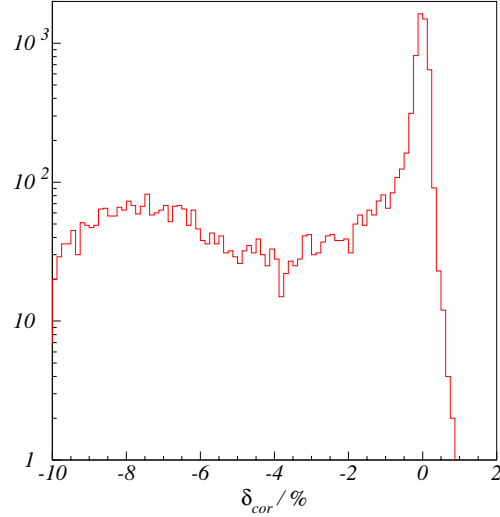


Figure 31:  $\delta_{cor}$  distribution of kin VI. Calorimeter, TOF and  $dE/dx$  cut have been applied.

### 3.5 Trigger Efficiency

Coincidences can be lost due to inefficiencies in the scintillator paddles and drift chambers of HMS or in the detectors on the hadron side.

The electron trigger only required 3 out of 4 scintillator planes to fire. For each plane the efficiency was determined to be greater than 99.5%. The total efficiency of the trigger was therefore

$$\varepsilon_{\geq 3/4} = \varepsilon_{3/4} + \varepsilon_{4/4} = \binom{4}{3} 0.995^3 (1 - 0.995) + 0.995^4 = 0.99985. \quad (28)$$

The intrinsic efficiencies of the three hadron detectors S1, S2 and T1+T2 were determined following the procedure used for the HMS. No correction

	S2	S1	T1+T2
$\varepsilon / \%$	$99.95 \pm 0.05$	$99.86 \pm 0.14$	$99.95 \pm 0.05$

Table 8: Deuteron detector efficiencies.

for trigger inefficiency was applied.

### 3.6 Tracking Efficiency

Each chamber had two planes measuring the horizontal position y and four planes measuring primarily x. The final momentum and angular resolution

(Table 6) were given by the combination of drift chamber resolution, error in the vertex reconstruction, multiple scattering effects, wire position uncertainties and errors in drift chamber positions and angles.

The tracking efficiency is the ratio between “good” events with a track and “good” events, which required

- a 3 out of 4 hardware electron trigger, as described earlier in Section 3.5.
- at least one hit inside and no hits outside the fiducial region of 3 out of 4 scintillator planes (Fig. 32). A plane fulfilling this condition was called “clean”. The fiducial region was in both hodoscopes given by the scintillator paddles 6–11 in  $x$  and 4–7 in  $y$ . The size and the location of the fiducial region were determined by maximizing the contribution from elastically scattered events while minimizing the contribution from non–elastically scattered events. For all kinematics more than 97% of elastically scattered electrons used in the final analysis were covered by the fiducial region.
- both good Čerenkov and calorimeter signals to reject all pions.
- a coincident deuteron, selected by a TOF and a ADC cut (Fig. 33).

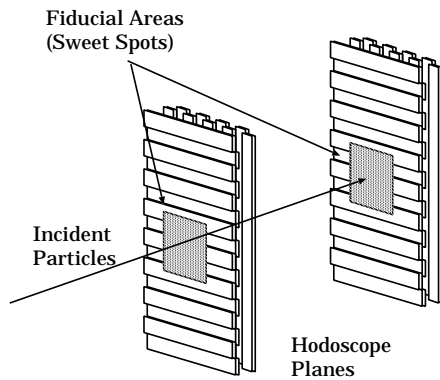


Figure 32: *Fiducial area as defined by scintillator planes of the HMS. There are 16 vertical (10 horizontal) paddles in  $x$  ( $y$ ) in total.*

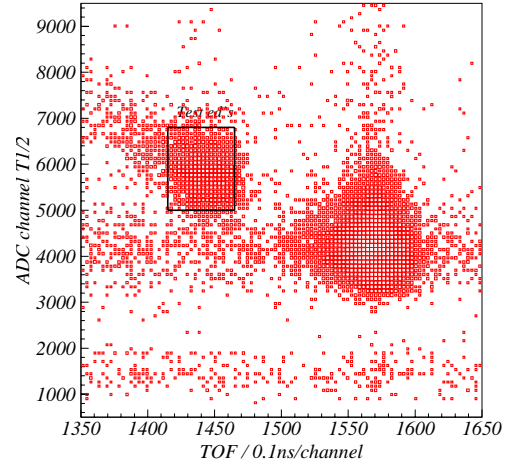


Figure 33: *TOF and ADC deuteron cut of  $D(e,e'd)$  run 15831 to kinematically constrain the focal plane illumination of coincident electrons.*

The tracking efficiency was checked by looking at its dependence on the size of the fiducial region and on the number of clean planes required (Table 9).

In the right column, the fiducial region was opened up completely; all 16 vertical and 10 horizontal paddles were in the fiducial trigger. The tracking efficiency did not drop below  $(97.5 \pm 0.35)\%$  for the largest fiducial area possible, regardless of the fiducial trigger used, because mainly the central part of the HMS acceptance was illuminated due to the kinematic constraint of elastic scattering; this restriction reduces edge effects. The tracking efficiency of the fiducial region used in the analysis (left column) drops to 97.5% when requiring no clean plane in the fiducial trigger (0/4). In this case the efficiency must be independent of the defined fiducial area; indeed, the results obey this requirement. At 3 or more clean planes, the tracking efficiency stabilizes. An increase of the fiducial area by a factor of 4 (middle column) does not change the tracking efficiency significantly.

Fid. Area x/y	6-11, 4-7			3-14, 2-9			1-16, 1-10		
Fid. trigger	0/4	<b>3/4</b>	4/4	0/4	3/4	4/4	0/4	3/4	4/4
$\varepsilon_{tr}$ / %	97.5	<b>98.5</b>	98.5	97.5	98.3	98.4	97.5	97.5	97.5

Table 9: *Tracking efficiencies  $\varepsilon_{tr}$  of  $D(e, e'd)$  run 15831 as a function of the size of the fiducial region and the number of clean scintillator plane signals in the fiducial trigger. For example a fiducial trigger labelled 3/4 means that the event must have 3 or more clean planes. Statistical error  $< 0.35\%$ .*

The reliability of the tracking algorithm was ensured by looking at the variations of the corrected electron yields  $\frac{\#e^-}{\varepsilon_{tr}}$  while changing the various tracking criteria, e.g. varying the maximum number of hits between 15 and 35. The yield varied around the mean within a range of less than 0.1%. The systematic tracking uncertainty was determined by looking for wrong decisions<sup>2</sup> of the tracking algorithm using the single event display (SED) [52]. No tracking error was found while checking 500 electrons of the  $D(e, e'd)$  run 15831 event by event which gave an upper limit of the systematic uncertainty of 0.2%. To get the total tracking uncertainty of 0.4%, the statistical error of 0.35% and the systematic uncertainty of 0.2% were added in quadrature. The fiducial efficiencies varied between 98.0% and 99.4%.

### 3.6.1 Wrong $y'_{fp/tar}$ Selection

There were some events which could not be reconstructed because of poor track information. Some electrons did not produce hits in all six planes of a

<sup>2</sup>It was looked whether the tracking algorithm found a track when it was supposed to, not necessarily the correct track, and whether it did not find a track when it was not supposed to.

chamber. As one  $y$  information per chamber is needed to form a track, we requested at least five out of six planes to fire. If a single plane had more than 25 hits, a track was not fit. It was checked with the SED (Fig. 34) that the inefficiency of the chambers was mainly caused by events where all 16 channels of a discriminator card, due to noise, fired or where a knock-on electron produced another short track and therefore clusters of wires were firing in one chamber. Since both of these conditions occurred for good electrons, these losses were corrected for (Sec. 3.6).

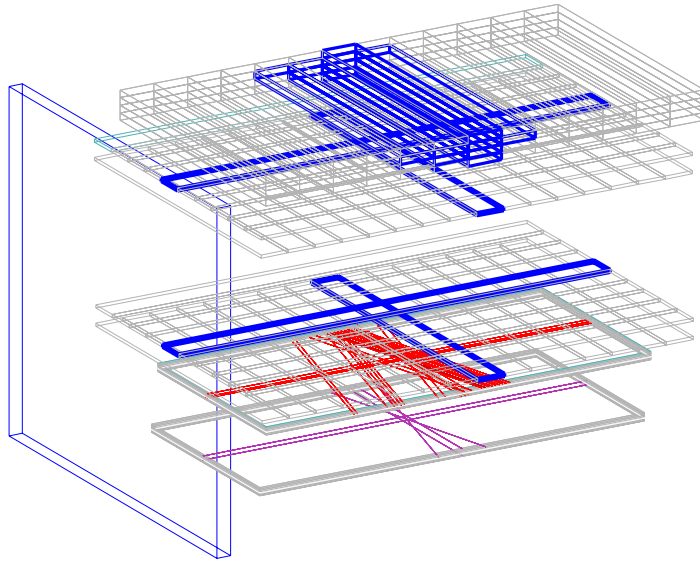


Figure 34:  $D(e, e'd)$  electron of run 15831, passing through the detectors from bottom (DC1 and DC2) via hodoscopes to top (Pb glass calorimeter). The tracking algorithm would not have been able to resolve the ambiguities caused by ringing cards in the  $u$  and  $v$  planes of DC2. The event was ignored. The lost electron had to be corrected for.

In the  $y'_{tar}$  spectras, tails reaching to  $\pm 50$ mrad were observed (Fig. 36), caused by events with badly reconstructed  $y'_{fp}$  information. Figure 35 shows that a ringing card in the second  $y$  plane of DC1 had mislead the algorithm. The blue track, with the bigger  $\chi^2$ , was not selected. A close examination with the SED revealed that the blue track should have had precedence over the red one.

In up to 0.3% of all HMS triggers, the tracking algorithm found more

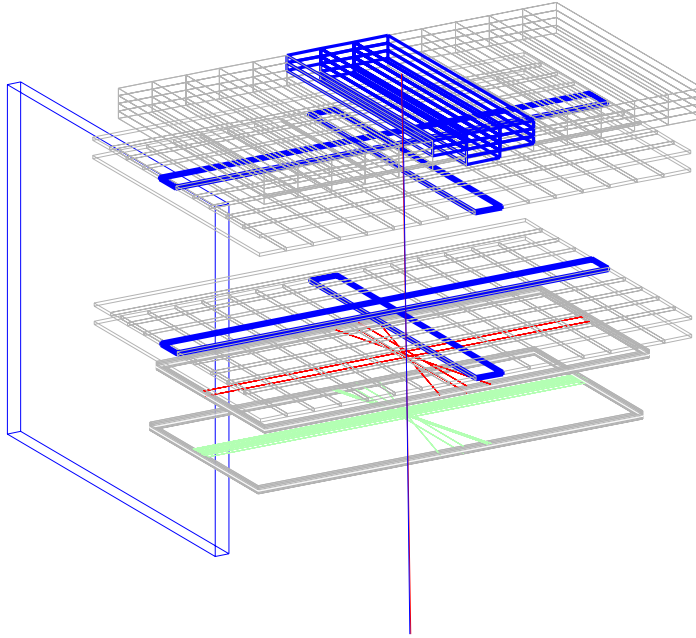


Figure 35: *Run 15831, the electron passed from bottom to top DC1 and DC2, two hodoscopes and Pb glass calorimeter. As the  $y'$  plane of DC1 had noisy wires, the algorithm found two tracks selecting the one with the lowest  $\chi^2$  (red). This selection is wrong.*

than one track. The ambiguities were mostly caused by multiple ringing  $y$  cards and therefore badly reconstructed  $y'_{fp/tar}$  informations. For such events the  $x'_{fp/tar}$  would be unaffected by such behaviour. In all these cases the track with the lowest  $\chi^2$  was chosen. This led to tails in both  $y_{tar}$  and  $y'_{tar}$ . As the small collimator and the short cryo targets constrained the electrons to illuminate only the central part of the focal plane, no cut on any reconstructed quantity other than  $\delta$  was applied to the data. The wrong  $y_{tar}$  and  $y'_{tar}$  informations did not affect the results as they are not used in the analysis.

### 3.7 Aluminum Target Window Subtraction

In order to remove counts coming from the aluminum endcaps of the cryo targets, data were taken with a “dummy” target of identical length and 9.3 times thicker windows (to get a similar luminosity). The luminosity normalized dummy counts were then subtracted from the regular data. The

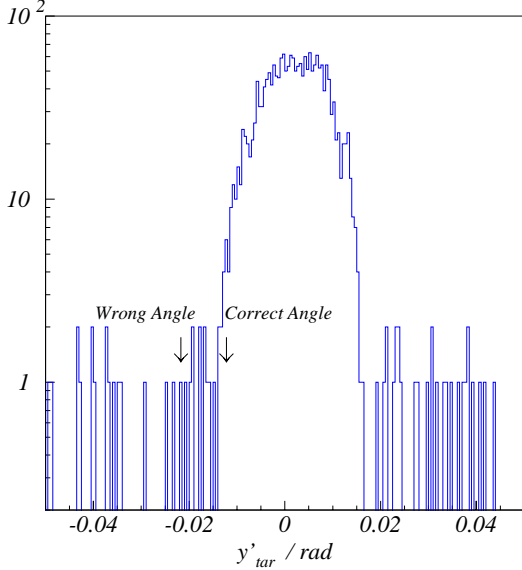


Figure 36:  $y'_{tar}$  distribution of run 15831. The reconstructed track from fig. 35 (red) has a  $y'_{tar}$  direction of  $-29$  mrad. The correct (blue) track corresponds to a  $y'_{tar}$  angle of  $-12$  mrad.

aluminum background varied between 0.2–1.1% for coincidence runs and 0.3–4.9% for  $H(e,e')$  data (Fig. 37 and 38). The systematic uncertainty was too small to be considered.

### 3.8 Correction for finite acceptance and extended target

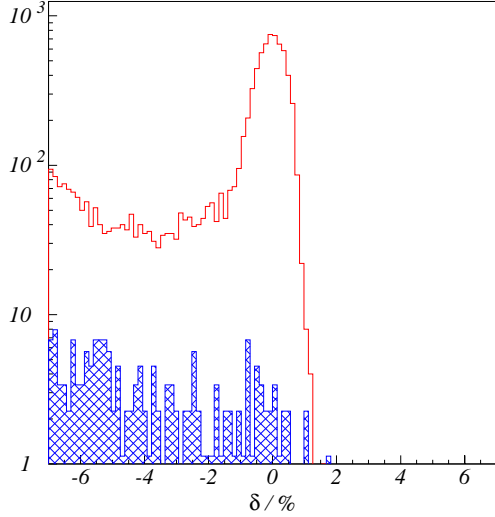
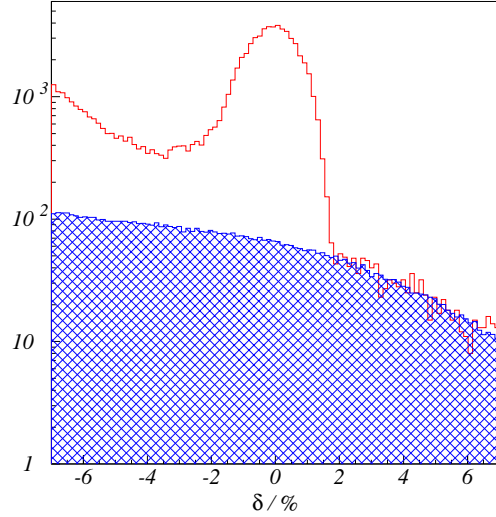
To compare to theory and other data, it is necessary to correct the cross section measured over an experiment-specific finite acceptance and extended target to that of a pointlike acceptance and target. Therefore every  $i^{\text{th}}$  bin of the  $\vartheta$ -distribution corresponds to a different  $\frac{d\sigma}{d\Omega}(\vartheta_i)$ .

By integrating over the target length  $l$  as well as the solid angle  $d\Omega$ , the correction factor  $c$  was calculated:

$$c = \frac{\int \int \int \frac{d\sigma}{d\Omega}(\vartheta(l, x', y')) dl dx' dy'}{\int \int \int \frac{d\sigma}{d\Omega}(\vartheta_o) dl dx' dy'}, \quad (29)$$

$$\text{with } \vartheta_o = \vartheta(l = 0, x' = 0, y' = 0) = \theta_{HMS}.$$

World data for  $A(Q^2)$  and  $B(Q^2)$  are used to calculate the differential cross sections in Eqn.29. The correction does not require an absolute knowledge of the cross sections. The correction factor  $c$  normalizes the cross section to both a point acceptance and a pointlike target. The product of the solid angle and the extended target acceptance for a specific kinematics is then given by  $ld\Omega/c$ .

Figure 37:  $Kin\ VI\ D(e,e'd)$  dummy subtraction.Figure 38:  $Kin\ VI\ H(e,e')$  dummy subtraction.

For the case where offsets in angle from the nominal one are present (known beam and target misalignments) these offsets can also be accounted for when calculating the numerator of Eqn.29. Table 10 gives the correction factors applicable for the case of the small collimator used for the cross section measurements. The correction increases when going to a longer target cell and a larger acceptance. The thickness of the collimator (6.345 cm) reduces

Label	0	I	II	III	IV	V	VI
$H(e,e'p)$	1.009	1.009	1.010	1.012	1.012	1.014	1.014
$D(e,e'd)$	-	1.018	1.017	1.017	1.020	1.028	1.029

Table 10: *Correction factor  $c$  taking into account all known offsets.*

the correction factor by less than 0.05% in the case of  $D(e,e'd)$  (0.01% for  $H(e,e'p)$ ). Table 11 shows the correction factors calculated for a pointlike

Label	0	I	II	III	IV	V	VI
$H(e,e'p)$	1.009	1.009	1.009	1.011	1.011	1.013	1.013
$D(e,e'd)$	-	1.015	1.015	1.015	1.0180	1.024	1.024

Table 11: *Correction factor  $c$  calculated similarly to Table 10, but requiring a point target ( $l=0$ ). 1.2 mrad beam angle correction is again included.*

target. As the target offsets along the beam are small (Table 4) and therefore negligible, the correction factors displayed in Table 11 originate from the finite solid angle only. The correction has a relative error of 10% including the solid angle uncertainty.

The nominal solid angle  $d\Omega$  is given by the dimensions of the collimator and its distance from the target (Eqn.30).

$$d\Omega = \frac{2 \times 1.011\text{cm} \times 2 \times 5.621\text{cm}}{(127.6\text{cm})^2} = 1.396\text{msr} \quad (30)$$

### 3.9 Radiative Correction

A major drawback in the use of the electron as a probe of nuclear structure is its tendency to radiate during scattering processes. The radiative effects require corrections, which are (in principle) exactly calculable. Both the one-photon [53–55] and the two-photon [56, 57] exchange corrections have been derived. Unfortunately, there is little information available on the uncertainty of these calculations. Experimentally, one has checked the radiative corrections by extrapolating form factors to momentum transfer zero, where  $F(0)$  is known. These checks lead to an estimated accuracy of less than 1% [58].

8 layers of CEREX around target cell / cm	0.0051
air gap between chamber and HMS / cm	15
HMS entrance window (Kevlar/Mylar) / cm	0.0381/0.0127

Table 12: *Materials used for external radiative corrections calculations (See also Table 3, 4).*

Following equations II.6 and II.9 of [53], the one-photon exchange radiative corrections for both deuterium and hydrogen have been computed for  $\delta$  cuts between -1% and -10%. Tables 3, 4 and 12 list all materials of relevance for the radiative corrections. The calculations were split into pre- and post-scattering contributions. Preradiation was assumed to happen in the first half of the cryotarget ( $l_{tar}/2$ ).

The quality of the correction was checked by dividing the number of electrons in a  $\delta$  cut by the corresponding radiative correction. The yield stayed well within a  $\pm 1\%$  error band, the systematic uncertainty of the correction, over the full range of  $\delta$  cuts (Figs. 39 and 40). For kin IV–VI, where the TOF and the dE/dx cut are not 100% efficient anymore (Sec 3.3, Fig. 26–31), this

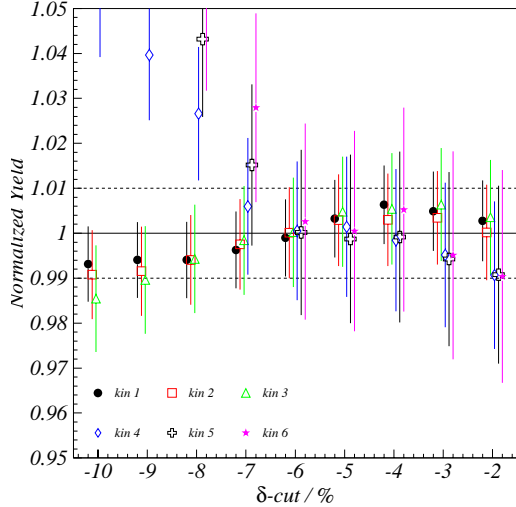


Figure 39: Quantitative check of radiative corrections for  $D(e,e'd)$  runs with statistical errors.

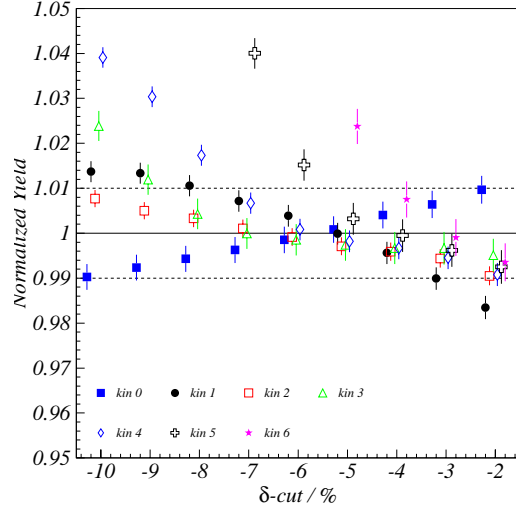


Figure 40: Quantitative check of radiative corrections for  $H(e,e')$  runs with statistical errors.

check is only valid for relatively tight  $\delta$  cuts ( $-2\%$  to  $-6\%$ ). Thus the  $\delta$  cut is needed to discriminate all e-p events.

Table 13 lists the multiplicative corrections for all our kinematics.

Label	$D(e,e'd)$	$H(e,e')$ and $H(e,e'p)$
0	N/A	0.8373
I	0.8354	0.8384
II	0.8341	0.8371
III	0.8323	0.8351
IV	0.8311	0.8339
V	0.8290	0.8259
VI	0.8217	0.8243

Table 13: Radiative correction factors calculated for a  $-4\%$   $\delta$  cut.

### 3.10 HMS/POLDER Acceptance Mismatch

The deuteron spectrometer (Fig. 22) has been optimized to focus the maximum number of deuterons on the  $H_2$  POLDER target located 44 cm behind S2. The deuteron distributions on S2 (Fig. 41), triggering scintillator for kin I-III, and on S1 (Fig. 42), shows that 1-3% of the deuterons were passing

outside the active region of S2/1 and therefore have been missing the trigger. These events had to be corrected for.

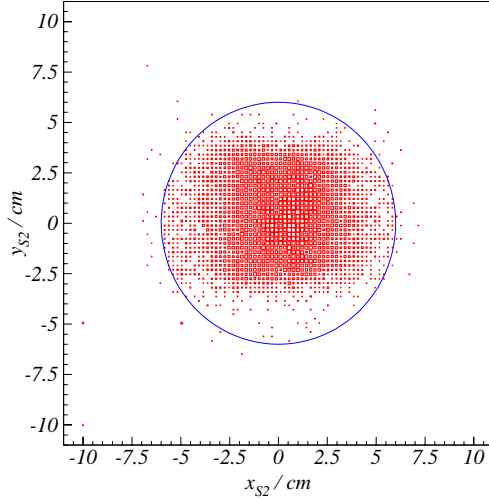


Figure 41: *Kin I deuteron distribution reconstructed at S2. Coordinate system: +x is horizontal towards bigger scattering angle, +y up. Circle indicates active area of scintillator S2 ( $r=6\text{ cm}$ ).*

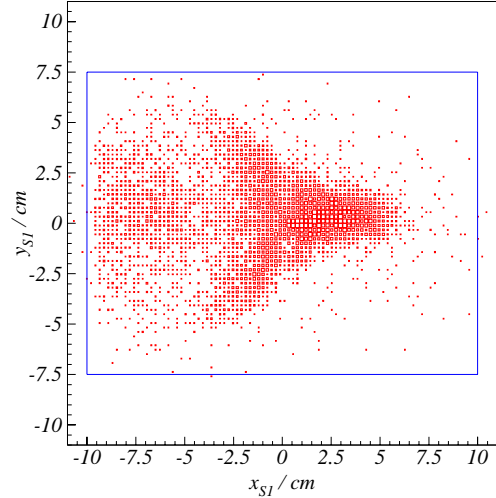


Figure 42: *Kin VI deuteron distribution reconstructed at S1. Coordinate system: +x is horizontal towards bigger scattering angle, +y up. Rectangle indicates active area of scintillator S1 ( $20 \times 15\text{ cm}^2$ ).*

For kin I, II, V and VI, the deuteron transmission factors were determined by simulating the deuteron channel phase space. A deuteron event generator (GLORIA, developed for [27,59]) and a ray-tracing code (SNAKE, [60]) were used. Both of the codes were extensively used during the design of the  $T_{20}$  experiment. The results are listed in table 14. On average, more than 90% of the loss occurred at S2, half of the remaining 10% were lost in the transport channel itself and the rest passed outside S1.

In the case of kin I+II, where no experimental verification was possible, the simulated corrections were used while for kin III and IV, the data were corrected with transmissions of 97.3% and 98.0%. For kin V and VI, the losses at S2 were measured and found to agree with the simulated results, therefore the measured transmissions were used. The good agreement between measured and simulated loss confirms that we have a fair understanding of the HMS/POLDER acceptance mismatch. The systematic uncertainty of 0.5% is added in quadrature to the statistical error of 0.5% of the measured loss leading to 0.8% total uncertainty of the correction.

Label	Simulated total Loss %	Measured Loss of S2 / %
I	97.3±0.2	N/A
II	97.2±0.2	N/A
III	N/A	N/A
IV	N/A	98.0±0.3
V	98.0±0.2	97.5±0.4
VI	96.4±0.2	96.0±0.5

Table 14: *Simulated total loss of deuteron channel and measured geometric inefficiency of S2 with statistical errors.*

### 3.11 Deuteron (and Proton) Absorption

To reach the POLDER detectors, deuterons (and protons for kin 0) had to pass through a number of different types and thicknesses of materials (Table 15). On their way, they could interact in various manners. The weakly bound nucleus could either break up, which means it would have been lost, or it could scatter elastically. In the latter case, if the scattering angle were small, the deuteron could survive. In the cryo target, where 2/3 of the hadron losses occur, the two processes were treated separately (Sec. 3.11.2). In all other materials, any interaction was equated with loss (Sec. 3.11.1), therefore  $\sigma_{\text{tot}} = \sigma_{\text{el}} + \sigma_{\text{inel}}$  was used.

Material	Thickness / cm	Density / g/cm <sup>3</sup>
Cryo target, D <sub>2</sub> or H <sub>2</sub>	4.11	0.167 or 0.723
Target cell wall, Al	0.0146	2.72
CEREX insulation, C <sub>12</sub> H <sub>24</sub> O <sub>3</sub> N <sub>2</sub>	0.0058	1.602
Kevlar, C <sub>65</sub> H <sub>63</sub> O <sub>12</sub> N <sub>3</sub> (I-V)	0.015	1.47
Mylar, C <sub>5</sub> H <sub>4</sub> O <sub>2</sub> (I-V)	0.0038	1.39
Al (VI)	0.02	2.72
Air gap, 80%N <sub>2</sub> , 20% O <sub>2</sub>	50	0.001293
He bag, Mylar	0.03	1.39
He gas	775	0.0001785
He bag, Mylar	0.03	1.39
Air gap	50	0.001293
S1 NE-102, C <sub>11</sub> H <sub>10</sub>	0.1	1.032

Table 15: *Materials used to calculate hadron losses. Beam offsets (Table 17) were added to the target thickness.*

### 3.11.1 Deuteron Loss occurring after the target

The inelastic cross section  $\sigma_{\text{inel}}$  is equal to the sum of diffraction ( $\sigma_{\text{diff}}$ ), proton and neutron stripping ( $\sigma_{\text{p/nstr}}$ ) and absorption ( $\sigma_{\text{abs}}$ ) cross sections (Tables 24–29).

Knowing the total cross section of all materials  $\sigma_i$ , the total loss  $\xi$  of deuterons can be written as

$$\xi = 1 - \sum_i e^{-\sigma_i l_i \rho_i \mathcal{N}_L / A_i} \simeq 1 - \sum_i (1 - (\sigma_i l_i \rho_i \mathcal{N}_L / A_i)) \quad (31)$$

with  $l$  the thickness,  $\rho$  the density,  $\mathcal{N}_L$  Avogadro's number and  $A$  the mol mass. For composite materials,  $\sigma$  was the weighted sum of the total cross section of every element, e.g. for Mylar ( $\text{C}_5\text{H}_4\text{O}_2$ ),  $\sigma_{\text{tot}} = 5 \times \sigma_{dC} + 4 \times \sigma_{dH} + 2 \times \sigma_{dO}$ .

### 3.11.2 Elastic d-d (p-p) Scattering in the Target

The elastic scattering in the target was treated differently. For the deuteron case, the angular distribution  $\frac{d\sigma}{d\Omega}(\theta)$  was taken from the Serber model (App. C), which takes into account the nuclear part of the elastic scattering only; and for the proton case it was taken from the partial wave analysis code SAID. For every origin  $z$  along the electron beam and all initial directions  $\vartheta$  and  $\varphi$ , the loss  $\xi(z, \vartheta, \varphi)$  of a hadron scattering elastically off a hadron in the target is

$$\xi(z, \vartheta, \varphi) = 1 - e^{-\sigma(z, \vartheta, \varphi) l \rho \mathcal{N}_L / A} \simeq \sigma(z, \vartheta, \varphi) l \rho \mathcal{N}_L / A \quad (32)$$

following Eqn. 31 with

$$\sigma(z, \vartheta, \varphi) = \int_{4\pi - acc(z, \vartheta, \varphi)} \frac{d\sigma}{d\Omega}(\theta) \sin \theta d\theta d\phi. \quad (33)$$

The integration of Eqn. 33 is performed over the entire sphere excluding the acceptance  $acc(z, \vartheta, \varphi)$  of the deuteron spectrometer, thus the limits of integration are a function of  $z$ ,  $\vartheta$  and  $\varphi$ .

The loss  $\xi(z, \vartheta, \varphi)$  was then folded with experimental hadron distributions  $n_{\text{sur}}(z, \vartheta, \varphi)$  in order to get the total loss

$$\xi_{\text{el}}^{\text{tar}} = \frac{\int \int \int \xi(z, \vartheta, \varphi) n(z, \vartheta, \varphi) dz d\vartheta d\varphi}{\int \int \int n(z, \vartheta, \varphi) dz d\vartheta d\varphi} \quad (34)$$

of elastically scattered hadrons.

The momentum of elastically scattered hadrons drops by 1.5% at a scattering angle of  $10^\circ$ . This shifted momentum is well within the momentum acceptance of POLDER, so that it is not necessary to modify the outlined calculation to take it into account.

Label	0	I	II	III	IV	V	VI
$\xi_{\text{el}}^{\text{tar}} / \%$	0.03	0.86	0.67	0.41	0.30	0.17	0.12
$\xi_{\text{inel}}^{\text{tar}} / \%$	0.00	4.28	3.60	2.84	2.56	2.23	2.12
$\xi_{\text{tot}}^{\text{rest}} / \%$	0.63	1.56	1.52	1.46	1.15	1.09	1.01
$\xi_{\text{tot}} / \%$	0.66	6.70	5.79	4.71	4.01	3.49	3.35

Table 16: *Total losses of protons (Kin 0) and deuterons.*  $\xi_{\text{el}}^{\text{tar}}$  is the loss of elastically scattered hadrons in the target,  $\xi_{\text{inel}}^{\text{tar}}$  is the inelastic loss in the target,  $\xi_{\text{tot}}^{\text{rest}}$  is the total loss in all other materials except the target.

Table 16 gives an overview of the different losses calculated. The deuteron cross section calculations (App. C) have a relative systematic uncertainty of 20% [61] which is the uncertainty of the deuteron absorption correction. The proton absorption is based on proton–nucleus cross section data found in [62–64] and a SAID calculation of the angular distribution of elastic p–p scattering. The relative uncertainties of the total reaction cross section measurements, and thus the uncertainties of the proton absorption correction, are  $<5\%$ .

### 3.12 Beam Angle and Offset

A picture of the  $\text{H}_2$  cell exit window (Fig. 43), exposed to beam during this and the following experiment, clearly indicated both a vertical and a horizontal offset in the beam position.

Figure 43: *Picture of  $\text{H}_2$  target exit window when looking upstream.* The radius of the inner (middle) circle is 2.12 (6.35) mm. The large brown square shows discolouring caused by the beam.



Using three Superharp scans (Table 17), we could determine an average beam position and direction at the target which were in good agreement

with the offsets of the large discoloured spot visualized in the exit window picture. The consistency of the offsets was later double checked and verified with  $W^2$ -plots (Fig. 44 and 45). The Superharps have been surveyed with an accuracy of  $200\text{ }\mu\text{m}$ . This leads to an angular uncertainty of  $0.3\text{ mrad}$  and a position uncertainty at the target of  $0.5\text{ mm}$ .

Scan	Position Offset / mm		Angular Offset / mrad	
	y	x	$y'$	$x'$
04/14/1997	2.5	-2.0	1.1	-1.5
08/20/1997	1.8	-1.9	0.7	-0.9
09/12/1997	2.0	-1.6	0.8	-1.2
Mean offsets	2.1	-1.5	0.9	-1.2

Table 17: *Beam position and direction at the target, determined with Superharp scans. Coordinate system assumed: positive x for beam left, positive y for vertically up.*

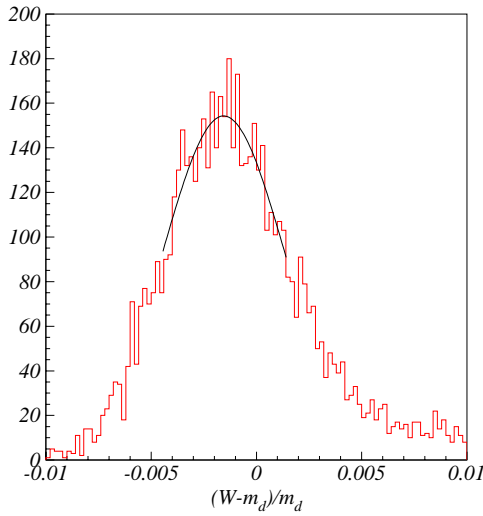


Figure 44: Invariant mass of  $D(e, e'd)$  kin VI.

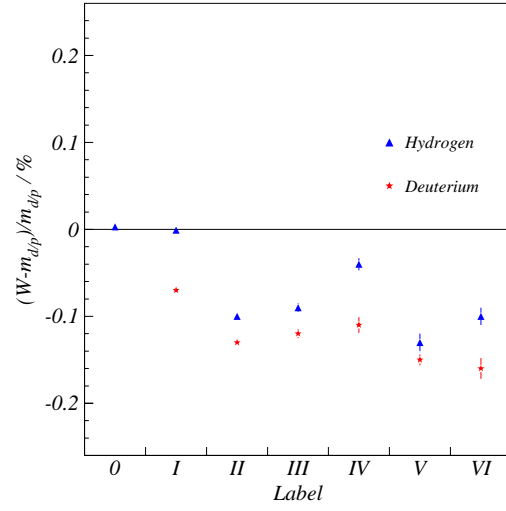


Figure 45: Relative ratios of invariant masses with statistical errors. The systematic uncertainty is 0.26%.

Fig. 45 shows the relative deviations between the invariant mass  $W$  and the target mass, which should be 0 for elastic scattering, plotted for each kinematic setting. Propagating through the systematic uncertainties of  $\Delta E/E = 1.2 \times 10^{-3}$ ,  $\Delta p'/p' = 1.1 \times 10^{-3}$  and  $\Delta \theta = 1\text{ mrad}$  results in an absolute system-

atic error  $\Delta W$  in the order of 5 MeV or 0.26%, which is almost two times larger than the maximum offset encountered (kin V+VI, Fig. 45).

### 3.13 Spectrometer Angle

In the scattering angle range of the experiment ( $20^\circ$ – $35^\circ$ ) the optical axis of the HMS was mispointing by  $<0.4$  mm while the magnets showed a maximum displacement of 0.3 mm [37] which is neglectable. Inclusive  $H(e,e')$  scans had been performed to calibrate the HMS angle. The angular offsets determined by the scans are  $<0.9$  mrad [43]. To get the total systematic uncertainty of the scattering angle of 1.0 mrad, the beam (Section 3.12) and the HMS angle uncertainty were added in quadrature.

### 3.14 Systematic Uncertainties

Here the systematic uncertainties, mentioned elsewhere in this work, are summarized. The sources of uncertainty, shown below in table 18, were added together in quadrature to estimate the total systematic uncertainty, listed in table 19.

	D(e,e'd)	H(e,e')	Section
Charge Measurement	0.4	1.0	2.3.2
Beam Energy, $\Delta E/E = 1.2 \times 10^{-3}$	0.76-1.39	0.75-1.82	2.3.4
Target Density/Boiling/Purity	0.5/0.5/0.3	0.5/0.5/0.0	2.3.5
PID Efficiency, Tracking	0.4	0.4	2.4,3.6
Scattering Angle, $\Delta\theta = 1$ mrad	1.6-3.4	1.5-3.8	3.13
Acceptance and Target Correction	0.15	0.15	3.8
Radiative Correction	1.0	1.0	3.9
Acceptance Mismatch	0.8	0.8	3.10
Hadron Absorption	1.4-0.7	0.1	3.11
Computer Dead Time	0.2	0.2	3.4

Table 18: *Systematic uncertainties (in %) in the extraction of  $d\sigma/d\Omega$ .*

Label	0	I	II	III	IV	V	VI
D(e,e'd)	N/A	2.70	2.72	2.82	2.96	3.50	4.16
H(e,e')	2.47	2.35	2.55	2.94	3.24	3.90	4.53

Table 19: *Total systematic uncertainty (in %) data.*

## 4 Results and Discussion

In the following three Subsections,  $H(e,e')$ ,  $D(e,e'd)$  elastic cross sections and  $A(Q^2)$  values are presented.

The beam energies quoted have been corrected for energy loss. The scattering refers to the center of the target. The values for  $E_{loss}$  are listed in Table 20.

	$D(e,e'd)$	$H(e,e')$
$E_{loss}$ / MeV	0.902-0.931	0.802-0.835

Table 20: *Calculated energy loss of the electron beam before interaction.*

### 4.1 Electron-Proton Elastic Cross Sections

At each kinematical setup,  $H(e,e')$  data were taken. In addition, one  $H(e,e'p)$  elastic cross section (kin 0) was measured. Results are listed in Table 21.

Label	$E$ GeV	$\theta$ deg	$d\sigma/d\Omega$ nb/sr	$\Delta_{stat}$ %	$\Delta_{syst}$ %
0	1.6447	23.62	268.80	0.3	2.7
I	1.4110	35.82	40.30	0.3	2.6
II	1.6447	33.58	31.24	0.2	2.8
III	2.0971	29.93	20.01	0.4	3.2
IV	2.4455	27.63	15.14	0.3	3.5
V	3.2468	23.36	10.24	0.4	4.2
VI	4.0451	20.33	7.85	0.4	4.8

Table 21: *Electron-proton cross section results.*

Figure 46 shows our cross section results relative to a fit. Having used the world's supply of  $\sigma_{e-p}$  data in a range of  $0.03 (GeV/c)^2$  around the desired  $Q^2$ , an L/T two parameter fit was performed [65]. Recent models are also plotted relative to the fit. The agreement is good and verifies that we have a reliable understanding of the systematic effects of the experiment.

### 4.2 Electron-Deuteron Elastic Cross Sections

Results and uncertainties are listed in Table 22. Figure 47 shows the ratio between our  $D(e,e'd)$  data points and a fit to previous and the JLab Hall C

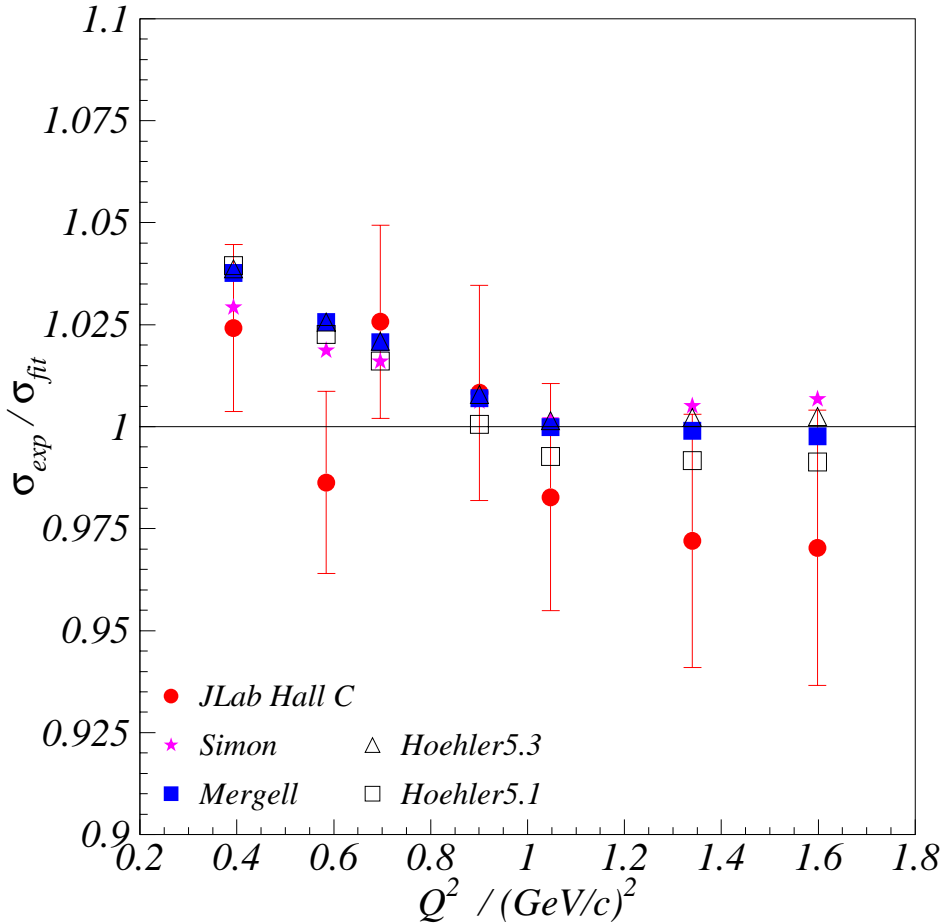


Figure 46: Electron-proton cross section results, normalized against a fit to previous data.

data which are on average 10% higher than the preliminary cross sections of the JLab Hall A experiment [66, 67]. The latter were not considered when having performed the fit. The data are further discussed in the following section.

### 4.3 Extraction of $A(Q^2)$

$A(Q^2)$  was extracted from the cross sections using the Rosenbluth formula (Section 1, Eqn. 8). Although  $B(Q^2)$  is at least one order of magnitude smaller than  $A(Q^2)$  and its contribution is further reduced by the  $\tan^2(\theta_e/2)$  factor, it was subtracted using  $B(Q^2)$  values from a fit to the world data [71]. The results are listed in Table 23. Fig. 48 shows our  $A(Q^2)$  values relative to a fit to previous data. Our results are in agreement with all but the lowest

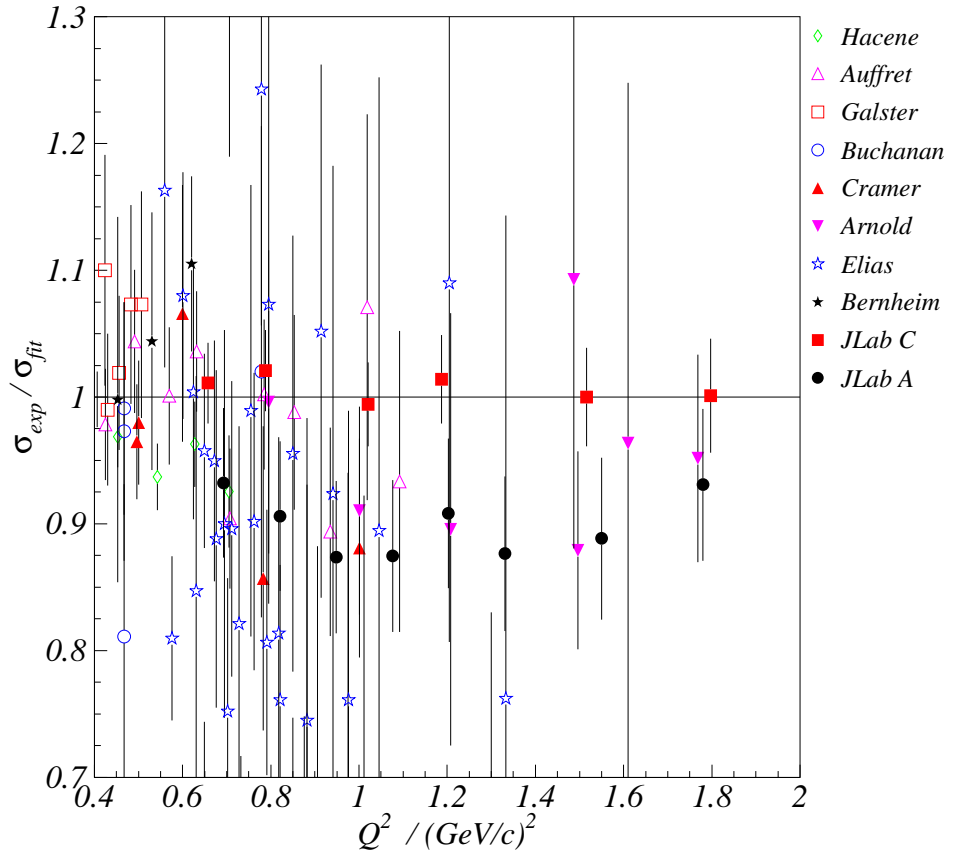


Figure 47: *Electron-deuteron cross section results, normalized against a fit to previous [10, 12–14, 16, 68–70] and the JLab Hall C data. The JLab Hall A data [66, 67] were not included when having performed the fit.*

SLAC data point (Arnold *et al.*) [14] smoothly approaching the DESY data (Galster *et al.*) [13] towards lower  $Q^2$ . They are  $\sim 5\%$  higher than the two highest  $Q^2$  points of the ALS experiment (Platchkov *et al.*) [17]. Our results clearly disagree with the CEA (Elias *et al.*) [12] and the preliminary JLab Hall A [66, 67] data, which are  $\sim 10\%$  lower than our results over the whole  $Q^2$  range covered by our experiment. The CEA data were measured with background contributions which might have been overestimated (Fig. 49).

Label	$E$ GeV	$\theta$ deg	$d\sigma/d\Omega$ pb/sr	$\Delta_{stat}$ %	$\Delta_{syst}$ %
I	1.4109	35.82	76.04	0.8	3.1
II	1.6446	33.58	42.68	0.8	3.1
III	2.0970	29.93	18.97	0.9	3.2
IV	2.4454	27.63	11.71	1.0	3.3
V	3.2467	23.36	4.75	0.9	3.8
VI	4.0450	20.33	2.46	1.1	4.4

Table 22: *Electron-deuteron cross section results.*

Label	E GeV	$\theta$ deg	$Q^2$ (GeV/c) $^2$	$\sigma_{\text{Mott}}$ nb/sr	$B(Q^2)$ $\times 10^{-6}$	$A(Q^2)$ $\times 10^{-6}$	$\Delta A_{stat}$ %	$\Delta A_{syst}$ %
I	1.4109	35.82	0.659	230.795	53.125	323.9	0.8	3.1
II	1.6446	33.58	0.788	220.088	22.289	191.9	0.8	3.1
III	2.0970	29.93	1.021	215.326	4.5754	87.78	0.9	3.2
IV	2.4454	27.63	1.187	218.877	1.7093	53.38	1.0	3.3
V	3.2467	23.36	1.513	245.884	0.2623	19.31	0.8	3.8
VI	4.0450	20.33	1.797	278.936	0.0062	8.823	1.1	4.4

Table 23: *Overview of extracted  $A(Q^2)$  values. The  $B(Q^2)$  values come from a fit to the world data [71].*

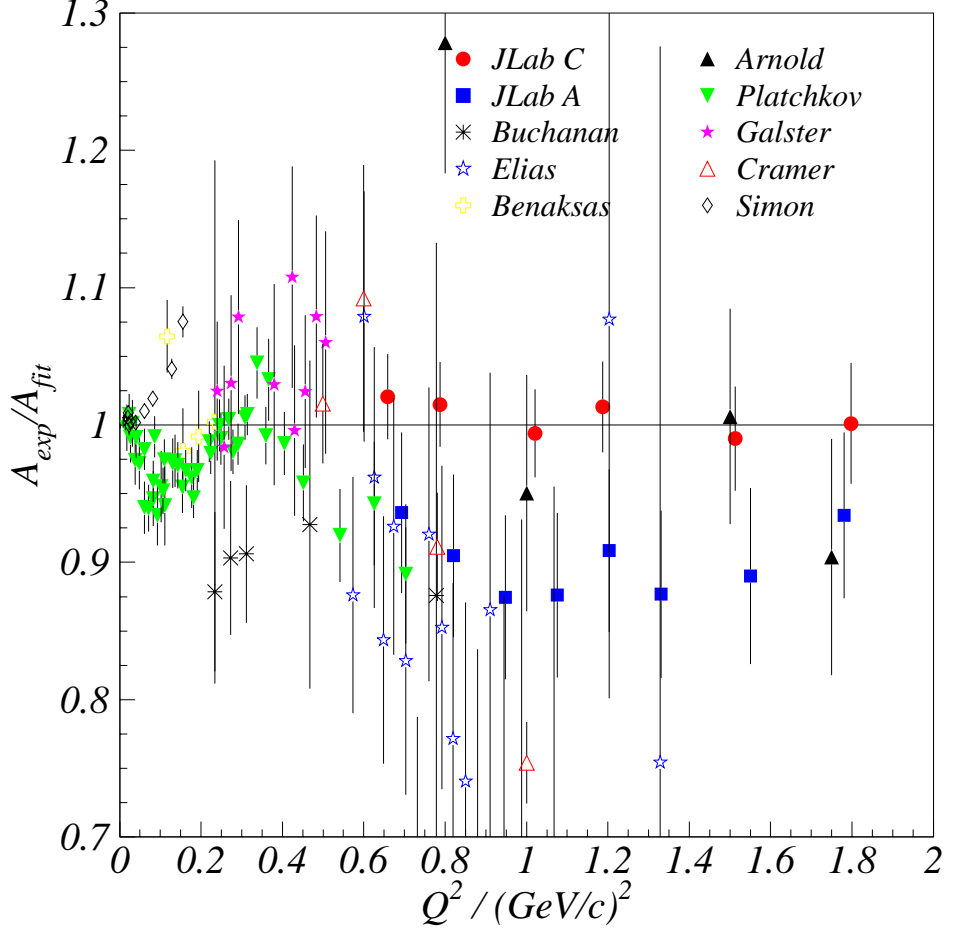


Figure 48:  $A(Q^2)$  data ( $\bullet$  present experiment) [10–17, 66, 67] relative to a fit to previous and the JLab Hall C data. The fitting procedure is described in [71, 72].

Figure 49: Deuteron momentum distribution at  $Q^2 = 0.63$  and  $0.88(\text{GeV}/c)^2$ . The deuteron was detected in a spectrometer while the coincident electron was tagged by a lead–Lucite shower counter [12]. Using the calculated width of the elastic peak, the authors estimated the (unspecified) background, indicated by the straight lines, which was subtracted.

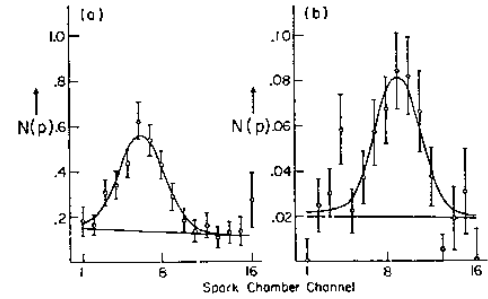


FIG. 3. Examples of deuteron elastic peak data. The momentum spectrum  $N(p)$  of the deuteron elastic peak at momentum transfers of  $4.0$  and  $4.75 \text{ F}^{-1}$  measured over a single angle bin are shown in arbitrary units, with momentum  $p$  denoted by spark-chamber channel number. The data have been corrected for the efficiencies of the spark chamber. The solid lines show fits of the resolution and background functions to the data.

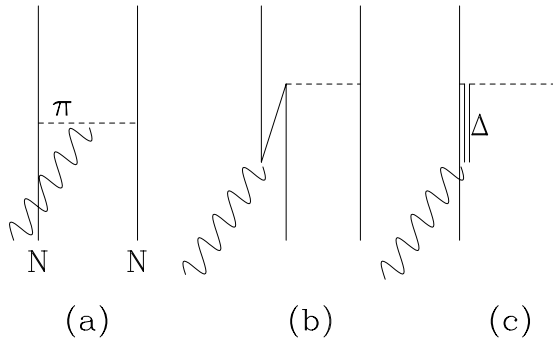
## 4.4 Comparison with Theory

Much theoretical work has been devoted to the calculation of the deuteron structure functions. This allowed for testing descriptions of the MECs, extracting the electric form factor of the neutron, looking for other degrees of freedom such as nucleon–resonances or quarks and understanding relativistic effects. Our data are going to be compared to some recent nonrelativistic and relativistic model calculations in the following sections.

### 4.4.1 Nonrelativistic Calculations

In the impulse approximation (IA), a virtual photon is exchanged between the electron and an individual nucleon within the nucleus. The electromagnetic form factors of the nucleon are assumed to be the same as for free nucleons. Nonrelativistically, the coupling of the photon to the charges yields to the form factors as Fourier transformations of the appropriate densities (Eqn. 8).  $A(Q^2)$  has been calculated in the NRIA for various NN potential models. In a nonrelativistic limit field–theoretical language, the NN potential is derived from an effective Lagrangian by fitting  $np$  data for  $T = 0$  states and  $np$  and  $pp$  data for  $T = 1$  states. The isospin dependence of the NN interaction

Figure 50: *The current produced by meson exchange: (a) the meson-in-flight current, (b) the pair term current, (c) The first-order contribution to the two-body electromagnetic current operator from the  $\Delta$  resonance in the intermediate state.*



is introduced by the exchange of isospin-1 particles between nucleons. To these IA results the contributions of MECs have been added. While isovector  $\pi$ - and  $\rho$ -MEC contributions (Fig. 50) are model independent and can be derived from the NN potential, isoscalar  $\pi\rho\gamma$ -MECs depend purely on the phenomenological approach. Another MEC contribution which is not directly related to the NN potential comes from the isobar excitation in the two-nucleon system. Recent models also apply relativistic corrections.

The NN potentials the JLab Hall C data are compared with (Fig. 51) have been developed over the past fifteen years. They all incorporate the main features of the NN scattering data. As phaseshift equivalence does not imply equal potentials or wave functions, the predicted structure functions

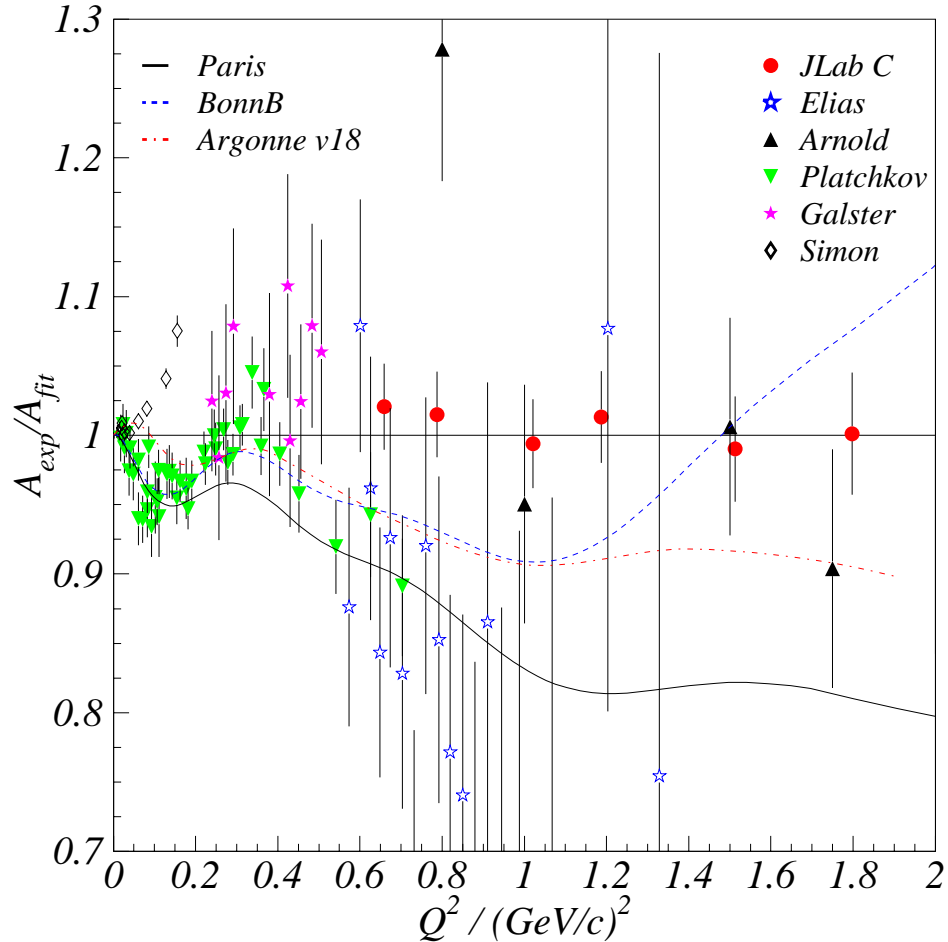


Figure 51:  $A(Q^2)$  results compared to nonrelativistic model calculations [18, 19, 21, 73–75], discussed in the text. For clarity only previous data from [12–15, 17] are shown.

do still differ (by 20%). The data agree best with calculations using the Argonne *v18* potential [75] which is an extended version of the *v14* potential. It has a charge-independent as well as a charge-independence breaking part and is fit to the binding energy,  $pp$ ,  $np$  and low-energy  $nn$  scattering data. The Höhler parametrization is used for the nucleon form factors. The fact that the *v18* curve is  $\sim 10\%$  lower than the JLab Hall C data implies that the nonrelativistic picture with perturbatively added MEC and relativistic corrections might still be incomplete. A 30% change of the electric form factor of the neutron would result in a 6% change in  $A(Q^2)$  in the  $Q^2$  range presented.

#### 4.4.2 Relativistic Calculations

At the  $A(Q^2)$ 's of interest here nuclear systems are probed with energy and momentum transfers comparable to the nucleon mass. The “usual” nonrelativistic description of the nucleus may no longer be reliable. Relativistically covariant models have to be developed. In Fig. 52 the data are compared with a relativistic quasipotential one–boson–exchange model (RIA) of Hummel and Tjon [22, 76] and a solution of the Bethe–Salpeter equation using the Gross approximation (CIA) of Van Orden, Divine and Gross [77]. The RIA used Höhler nucleon form factors while the CIA curves were calculated with quark model form factors [78]. Results of a very recent RIA calculation from Phillips and Cohen [79, 80] using an equal–time formalism are also shown. The nucleon form factors used come from Mergell, Meissner and Drechsel [81]. The agreement between the full model calculations (MEC included) and the data is reasonable. The three full calculations agree within 20% and the curves are of similar shape.

## 5 Summary

In Hall C of JLab, we have successfully performed a measurement of the longitudinal structure function  $A(Q^2)$  in the momentum transfer range between 0.66 and 1.8  $(\text{GeV}/c)^2$ . These new  $A(Q^2)$  data do resolve discrepancies between older data sets and will put significant constraints on models of the deuteron electromagnetic structure.

The  $A(Q^2)$  results were compared to theoretical models based on nonrelativistic (NRIA) and relativistic (CIA and RIA) impulse approximations with and without MECs included. The agreement between the full (MEC included) nonrelativistic calculations using the Argonne  $v18$  potential and our  $A(Q^2)$  data is good. The CIA and RIA predictions all underestimate the structure function over the whole  $Q^2$ –range of the experiment which indicates that they lack a good control of the different MEC contributions. Including the  $\pi\rho\gamma$  MECs leads for all theories to better agreement between data and theoretical calculations.

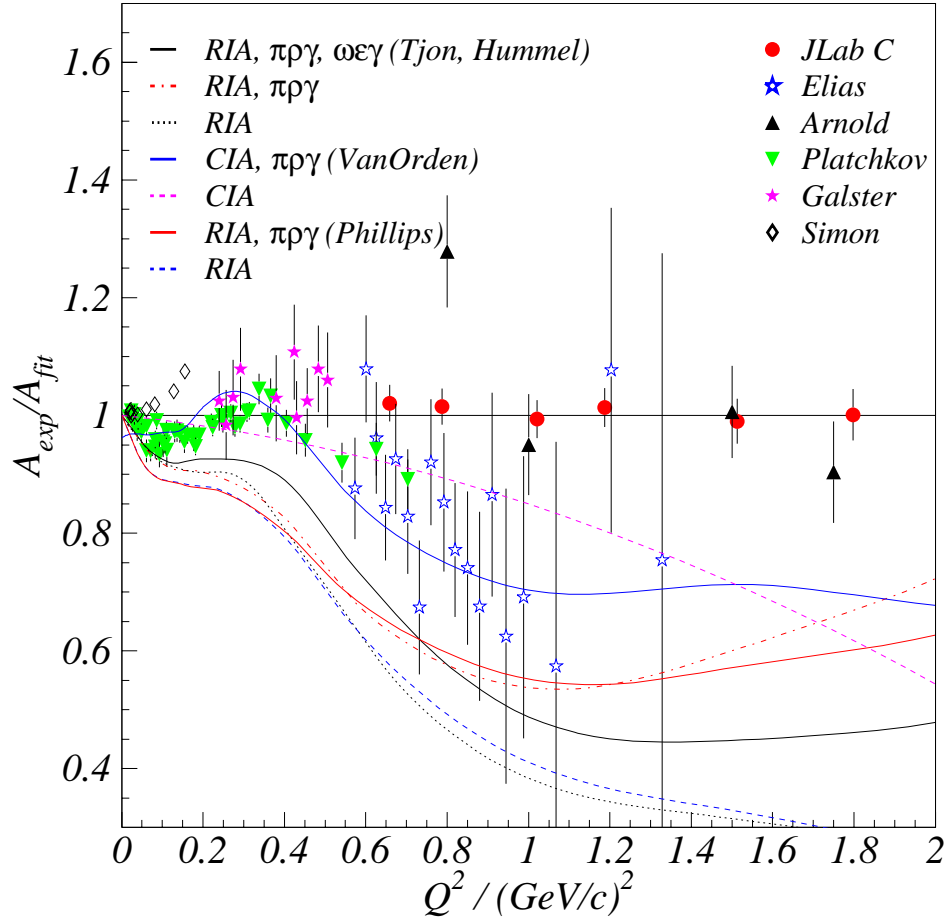


Figure 52:  $A(Q^2)$  results compared to relativistic model calculations [22, 76, 77], discussed in the text. For clarity only previous data from [12–15, 17] are shown.

## A Electronic Dead Time

When a trigger is received, the electronics sets a gate,  $t=30\text{ns}$  wide. During the time interval  $t$ , any incoming triggers, separated by less than  $30\text{ns}$ , are ignored.

Suppose the mean time between events is  $\tau$ . If an event opens a gate of width  $t$ , then the mean number of additional events which occurred during this gate is  $t/\tau$ . As the gate width is orders of magnitude smaller than the mean time between events, the number of gates  $N_{\text{meas}}$  is to first order slightly smaller than the total number of events  $N_{\text{tot}}$ :

$$N_{\text{meas}} = N_{\text{tot}} \cdot (1 - t/\tau). \quad (35)$$

Having used three additional scalers with gate widths 60, 90 and 120ns, we could easily determine the total number of events at  $t=0$ . During the experiment, electronic dead time corrections were always less than 0.5%.

## B Reduction of Kinematic Broadening

The only reconstructed quantity used for the extraction of the cross sections was  $\delta = \frac{p(\theta) - p_0}{p_0}$ . In order to improve the momentum resolution a correction was applied which eliminated kinematic broadening of the discrete momentum peak caused by the finite spectrometer angular acceptance and the angular dependence of the scattered electron energy. Starting with the known kinematic relation

$$p(\theta) = \frac{p_{beam}}{1 + \frac{2p_{beam}}{m_d} \sin^2 \frac{\theta}{2}}, \quad (36)$$

$p_{cor}$ , the corrected momentum, was first order Taylor-expanded in the following way:

$$p_{cor} = p(\theta) + \frac{1}{1!} \frac{d}{d\theta} p(\theta) \bigg|_{\theta} (\theta_0 - \theta) + \dots \quad (37)$$

$$\text{with } \frac{d}{d\theta} p(\theta) = -\frac{p^2(\theta)}{m_d} \sin \theta. \quad (38)$$

The corrected relative momentum  $\delta_{cor}$  then becomes

$$\delta_{cor} \simeq 100 \cdot \left( \frac{p_{cor}}{p_0} - 1 \right). \quad (39)$$

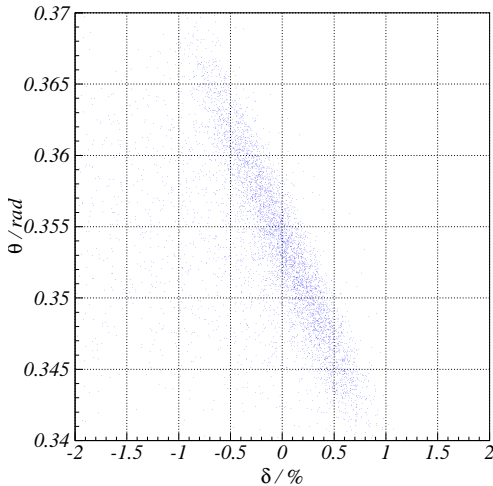


Figure 53:  $\delta$ - $\theta$  correlation of kin VI. Calorimeter, TOF and  $dE/dx$  cut have been applied.

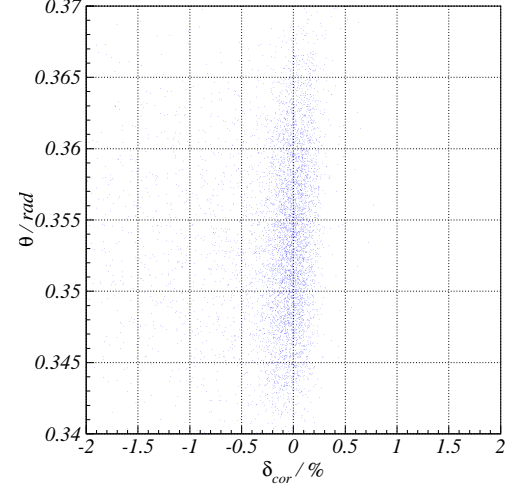


Figure 54:  $\delta_{cor}$ - $\theta$  correlation of kin VI. Calorimeter, TOF and  $dE/dx$  cut have been applied.

Fig. 53 and 54 show the  $\delta - \theta$  correlation before and after having applied the kinematic correction. The corrected momentum  $\delta_{cor}$  does hardly show a  $\theta$  correlation anymore.

## C Deuteron cross section calculations

### C.1 Theoretical Considerations

The different possible cross sections — elastic, diffraction, proton and neutron stripping and absorption — were calculated within the Serber model, developed by Serber [82] and Glauber [83] to describe the breakup of the deuteron. This model has in the recent past also been used successfully to describe the breakup of exotic nuclei — halo nuclei — which have properties, which are quite similar to the deuteron: weak binding energy and large spatial extension, see [84] and [61] and references therein.

In the Serber model, the interaction with the target is described by a so called profile function  $S_i(b)$  for the proton and the neutron, which depends only on the impact parameter  $b$ . In the eikonal approximation the profile function is given by integrating the interaction potential along the beam axis:

$$S(\vec{b}) = \exp \left[ \frac{-i}{\hbar v} \int dz V(\vec{b} + z\hat{z}) \right] \quad (40)$$

At the energies studied, it is assumed that the interaction potential is proportional to the density and the forward scattering amplitude:

$$V_n(r) = -\frac{1}{2} \hbar v [i + \alpha] (Z_T \sigma_{np} + N_T \sigma_{nn}) \rho(r). \quad (41)$$

Similarly, (by exchanging  $Z_T$  and  $N_T$ ) for  $S_n$  the profile function is given as

$$S_n(\vec{b}) = \exp \left\{ \frac{-1}{2} [1 - i\alpha] (Z_T \sigma_{np} + N_T \sigma_{nn}) \rho_t(b) \right\}, \quad (42)$$

with  $\rho_t(b)$  the density of the target integrated along the beam axis.

For the parameter  $\alpha$ , which is the ratio of the real to imaginary part of the forward scattering amplitude, we have used the parameterisation as given by [85], which is based on the SAID program. For the nucleon-nucleon cross section, we have used the parameterization of [86]. A similar Table of the  $\alpha$  parameters can also be found in [87]. For the densities of the targets we have used the tabulated values of [88].

For the deuteron wave function we have assumed a simple  $s$ -state wave function in a Wood Saxon potential ( $r_0 = 1$  fm,  $a = 0.5$  fm). The depth has been chosen to reproduce the experimental binding energy ( $B = 2.226$  MeV).

The different nuclear reaction processes can now be calculated in the following manner: The differential and total cross section for elastic scattering are given by

$$\frac{d\sigma_{\text{el.}}}{d^2 \vec{K}_\perp} = \frac{|a(\vec{K}_\perp)|^2}{(2\pi)^2}, \quad (43)$$

with

$$a(\vec{K}_\perp) = \int d^2 \vec{R}_\perp e^{-i \vec{K}_\perp \cdot \vec{R}} \int d^3 r \phi_0^*(\vec{r}) (S_p(b_p) S_n(b_n) - 1) \phi_0(\vec{r}) , \quad (44)$$

where  $b_p = R_\perp + r_\perp$ ,  $b_n = R_\perp - r_\perp$ , and

$$\sigma_{\text{el.}} = \int d^2 \vec{R}_\perp \left| \int d^3 r \phi_0^*(\vec{r}) (S_p S_n - 1) \phi_0(\vec{r}) \right|^2 . \quad (45)$$

The total interaction cross section consists of four different subprocesses: The inelastic scattering of the deuteron, also called *diffraction* is given by

$$\sigma_{\text{diff.}} = \int d^2 \vec{R}_\perp \left[ \int d^3 r \phi_0(\vec{r})^* |S_p S_n|^2 \phi_0(\vec{r}) - \left| \int d^3 r \phi_0(\vec{r})^* S_p S_n \phi_0(\vec{r}) \right|^2 \right] . \quad (46)$$

In addition there is absorption, where either the proton or the neutron reacts with the target and is therefore not seen in the forward direction. One can distinguish *neutron-stripping*, where the proton remains in the final state, *proton-stripping* with only the neutron in the final state and the *absorption* of both nucleons, that is, neither proton nor neutron in the forward direction. The respective cross section are

$$\sigma_{\text{n-str.}} = \int d^2 \vec{b}_n \left[ 1 - |S_n(\vec{b}_n)|^2 \right] \int d^3 r \phi_0(\vec{r})^* |S_p(\vec{b}_p)|^2 \phi_0(\vec{r}) \quad (47)$$

$$\sigma_{\text{p-str.}} = \int d^2 \vec{b}_p \left[ 1 - |S_p(\vec{b}_p)|^2 \right] \int d^3 r \phi_0(\vec{r})^* |S_n(\vec{b}_n)|^2 \phi_0(\vec{r}) \quad (48)$$

$$\sigma_{\text{abs.}} = \int d^2 \vec{b}_p \left[ 1 - |S_c(\vec{b}_p)|^2 \right] \int d^3 r \phi_0(\vec{r})^* \left[ 1 - |S_n(\vec{b}_n)|^2 \right] \phi_0(\vec{r}) \quad (49)$$

A simplification of the full Serber model has been used quite often: Here one defines a interaction potential for the whole deuteron. This approximation was used by [86] to describe the interaction of stable nuclei. In this approach we can no longer distinguish between the different interaction cross section mechanism. The *combined* profile function in this case is then given by folding the deuteron density with the interaction potential

$$V_D(r) = \int d^3 x \rho_D(x) V_N(|\vec{r} - \vec{x}|) . \quad (50)$$

and therefore

$$S_D(b) = \exp \left[ \frac{-1}{2} A_T (\sigma_{np} + \sigma_{nn}) \int d^3 x \rho_D(\vec{x}) \rho_t(\vec{b} - \vec{x}_\perp) \right] \quad (51)$$

For the deuteron density we have used a fit of the form

$$\rho_D(r) \sim \frac{r}{c_0 - c_1 r + c_2 r^2} \exp(-\lambda r) \quad (52)$$

with the parameters fitted to reproduce the density as calculated from the PARIS deuteron analytic wave function [89]. The elastic and interaction cross sections in this picture are given by

$$\frac{d\sigma_{\text{el.}}}{d^2\vec{K}_\perp} = \frac{|a(\vec{K}_\perp)|^2}{(2\pi)^2}, \quad (53)$$

with

$$a(\vec{K}_\perp) = \int d^2\vec{R}_\perp e^{-i\vec{K}_\perp \cdot \vec{R}} (S_D - 1) \quad (54)$$

and

$$\sigma_{\text{el.}} = \int d^2\vec{R}_\perp |S_D - 1|^2 \quad (55)$$

$$\sigma_I = \int d^2\vec{R}_\perp (1 - |S_D|^2) \quad (56)$$

The use of this approximation is well justified for strongly bound nuclei, but its use for halo nuclei has been criticized in [90], due to the correlation of the movement of halo-nucleon and core in this case. This critic is of course even more valid in the case of the deuteron. Detailed listings of all  $\sigma_{\text{tot}}(E)$  and  $d\sigma/d\Omega(\theta)$  distributions used are listed in App. C.

## C.2 Results of Deuteron Cross Section Calculations

Elastic as well as interaction cross sections, calculated using the (full) Serber model, and the total cross sections, calculated with the (simplified) Glauber model, are given in the Tables below.

Using the Serber model we are giving the decomposition of the interaction cross section into different absorption channels as well.

$E/A$ MeV	$\sigma_I$	$\sigma_{\text{el}}$	$\sigma_{\text{tot}}$	$\sigma_{\text{diff}}$	$\sigma_{\text{pstr}}$	$\sigma_{\text{nstr}}$	$\sigma_{\text{abs}}$
		mb			mb		
60	200.	67.0	267	26.0	75.1	75.1	24.62
88	158.	49.8	208	22.0	60.4	60.4	15.43
104	141.	42.1	183	19.4	54.9	54.9	12.55
135	119.	30.8	150	14.8	47.8	47.8	9.30
158	109.	24.9	134	12.1	44.5	44.5	7.98
202	97.6	17.6	115	8.74	41.0	41.0	6.71
239	93.1	14.1	107	6.99	39.9	39.9	6.30
280	91.2	11.7	103	5.83	39.6	39.6	6.20

Table 24: D(d,X) cross sections, calculated with the full Serber model.

$E/A$ MeV	$\sigma_I$	$\sigma_{el}$	$\sigma_{tot}$	$\sigma_{diff}$	$\sigma_{pstr}$	$\sigma_{nstr}$	$\sigma_{abs}$
		mb			mb		mb
60	275.	129.	404	43.0	90.8	90.8	50.4
88	234.	109.	343	39.5	79.5	79.5	36.3
104	217.	99.0	316	36.2	74.8	74.8	31.2
135	190.	79.5	270	29.4	68.2	68.2	24.8
158	176.	67.4	243	24.9	64.9	64.9	21.9
202	160.	50.4	210	18.5	61.3	61.3	19.0
239	153.	41.2	194	15.0	60.0	60.0	18.1
280	150.	34.8	185	12.6	59.7	59.7	17.9

Table 25:  $^4\text{He}(\text{d},\text{X})$  cross sections, calculated with the full Serber model.

$E/A$ MeV	$\sigma_I$	$\sigma_{el}$	$\sigma_{tot}$	$\sigma_{diff}$	$\sigma_{pstr}$	$\sigma_{nstr}$	$\sigma_{abs}$
		mb			mb		mb
60	556.	359.	915	57.6	163.	163.	173.
88	494.	328.	822	54.8	151.	151.	136.
104	465.	309.	774	51.4	146.	146.	121.
135	423.	269.	692	43.4	139.	139.	101.
158	400.	239.	639	37.7	135.	135.	91.9
202	372.	190.	562	28.9	130.	130.	82.0
239	360.	160.	520	23.8	129.	129.	78.5
280	355.	137.	492	20.1	128.	128.	77.7

Table 26:  $^{12}\text{C}(\text{d},\text{X})$  cross sections, calculated with the full Serber model.

$E/A$ MeV	$\sigma_I$	$\sigma_{el}$	$\sigma_{tot}$	$\sigma_{diff}$	$\sigma_{pstr}$	$\sigma_{nstr}$	$\sigma_{abs}$
		mb			mb		mb
60	612.	405.	1017	58.7	176.	176.	201.
88	545.	372.	917	56.3	164.	164.	159.
104	515.	352.	867	53.0	159.	159.	143.
135	469.	310.	779	45.1	152.	152.	120.
158	445.	278.	723	39.3	148.	148.	109.
202	415.	223.	638	30.3	143.	143.	98.2
239	403.	189.	592	25.0	141.	141.	94.3
280	397.	163.	560	21.2	141.	141.	93.3

Table 27:  $^{14}\text{N}(\text{d},\text{X})$  cross sections, calculated with the full Serber model.

$E/A$ MeV	$\sigma_I$	$\sigma_{el}$	$\sigma_{tot}$	$\sigma_{diff}$	$\sigma_{pstr}$	$\sigma_{nstr}$	$\sigma_{abs}$
		mb			mb		mb
60	682.	465.	1147	59.1	192.	192.	237.
88	608.	429.	1027	56.5	181.	181.	189.
104	575.	407.	982	53.1	175.	175.	169.
135	525.	360.	885	45.0	168.	168.	143.
158	498.	323.	821	39.2	164.	164.	130.
202	466.	260.	726	30.2	159.	159.	116.
239	453.	220.	673	24.9	157.	157.	112.
280	447.	190.	637	21.0	157.	157.	111.

Table 28:  $^{16}\text{O}(\text{d},\text{X})$  cross sections, calculated with the full Serber model.

$E/A$ MeV	$\sigma_I$	$\sigma_{el}$	$\sigma_{tot}$	$\sigma_{diff}$	$\sigma_{pstr}$	$\sigma_{nstr}$	$\sigma_{abs}$
		mb			mb		mb
60	897.	629.	1526	61.1	245.	239.	351.
88	805.	583.	1388	61.3	230.	224.	289.
104	766.	559.	1325	59.2	224.	218.	264.
135	709.	511.	1220	52.7	215.	210.	230.
158	678.	474.	1152	47.2	211.	206.	214.
202	641.	404.	1045	37.6	206.	201.	196.
239	625.	353.	978	31.5	204.	200.	189.
280	618.	312.	930	26.9	203.	200.	188.

Table 29:  $^{27}\text{Al}(\text{d},\text{X})$  cross sections, calculated with the full Serber model.

$E/A$ MeV	$\sigma_I$	$\sigma_{el}$	$\sigma_{tot}$
		mb	
60	99.6	46.1	145.
88	75.7	33.9	109.
104	67.4	28.4	95.8
135	57.0	20.3	77.3
158	52.4	16.2	68.7
202	47.7	11.3	59.0
239	46.1	8.98	55.1
280	45.7	7.47	53.2

Table 30:  $\text{H}(\text{d},\text{X})$  cross sections, calculated with the Glauber model.

$E/A$ MeV	$\sigma_I$	$\sigma_{el}$	$\sigma_{tot}$
		mb	
60	212.	97.2	309.
88	160.	67.4	228.
104	142.	55.0	197.
135	119.	38.1	158.
158	110.	30.0	140.
202	99.8	20.6	120.
239	96.4	16.2	112.
280	95.5	13.4	109.

Table 31: D(d,X) cross sections, calculated with the Glauber model.

$E/A$ MeV	$\sigma_I$	$\sigma_{el}$	$\sigma_{tot}$
		mb	
60	300.	190.	490.
88	242.	154.	396.
104	220.	134.	355.
135	192.	102.	294.
158	179.	84.7	263.
202	165.	61.0	226.
239	160.	49.0	209.
280	159.	41.0	200.

Table 32:  $^4\text{He}(d,X)$  cross sections, calculated with the Glauber model.

$E/A$ MeV	$\sigma_I$	$\sigma_{el}$	$\sigma_{tot}$
		mb	
60	598.	445.	1043.
88	509.	398.	908.
104	474.	371.	846.
135	427.	316.	744.
158	405.	277.	682.
202	381.	215.	596.
239	372.	179.	551.
280	370.	152.	523.

Table 33:  $^{12}\text{C}(d,X)$  cross sections, calculated with the Glauber model.

$E/A$ MeV	$\sigma_I$	$\sigma_{el}$	$\sigma_{tot}$
	mb		
60	656.	495.	1151.
88	562.	446.	1008.
104	525.	418.	943.
135	475.	361.	836.
158	451.	319.	770.
202	425.	251.	677.
239	416.	210.	626.
280	414.	180.	594.

Table 34:  $^{14}\text{N}(\text{d},\text{X})$  cross sections, calculated with the Glauber model.

$E/A$ MeV	$\sigma_I$	$\sigma_{el}$	$\sigma_{tot}$
	mb		
60	726.	554.	1281.
88	624.	502.	1126.
104	584.	472.	1056.
135	530.	410.	940.
158	504.	364.	868.
202	476.	288.	764.
239	466.	241.	708.
280	463.	207.	671.

Table 35:  $^{16}\text{O}(\text{d},\text{X})$  cross sections, calculated with the Glauber model.

$E/A$ MeV	$\sigma_I$	$\sigma_{el}$	$\sigma_{tot}$
	mb		
60	956.	745.	1701.
88	834.	678.	1512.
104	786.	644.	1430.
135	721.	580.	1301.
158	690.	532.	1223.
202	656.	447.	1104.
239	645.	387.	1032.
280	642.	339.	981.

Table 36:  $^{27}\text{Al}(\text{d},\text{X})$  cross sections, calculated with the Glauber model.

## References

- [1] D. Abbott *et al.* *Phys. Rev. Lett.*, 82/7:1379, 1998.
- [2] L. Eyraud. *Optimisation et calibration à SATURNE du polarimètre POLDER*. PhD thesis, Université de Joseph Fourier – Grenoble 1, 1998.
- [3] W. Zhao. *Tensor Polarization of the Deuteron at High Momentum Transfer in Elastic ( $e, d$ ) Scattering*. PhD thesis, MIT, 1999.
- [4] R.B. Wiringa *et al.* *Phys. Rev. C*, 51:38, 1995.
- [5] B. Frois and I. Sick, editors. *Modern Topics in Electron Scattering*, page 566. World Scientific Publishing, 1991.
- [6] H. Henning. *priv.com.*, 1995.
- [7] J. S. Real. *Polarimètre à deutons de recul de 175MeV à 500MeV*. PhD thesis, ISN Grenoble, 1994.
- [8] S. Kox *et al.* *Nucl. Instr. and Meth.*, A346:527–543, 1994.
- [9] K. Hafidi. *Strucutre electromagnetique du deuton*. PhD thesis, CEA/Saclay F-91191 Gif-sur-Yvette Cedex, 1999.
- [10] C.D. Buchanan and M.R. Yearian. *Phys. Rev. Lett.*, 15:303, 1965.
- [11] D. Benaksas, D. Drickey, and D. Frerejacque. *Phys. Rev.*, 148:1327, 1966.
- [12] J.E. Elias, J.I. Friedman, G.C. Hartmann, H.W. Kendall, P.N. Kirk, M.R. Sogard, L.P. Van Speybroeck, and J.K. de Pageter. *Phys. Rev.*, 177:2075, 1969.
- [13] S. Galster, H. Klein, J. Moritz, K.H. Schmidt, D. Wegener, and J. Bleckwenn. *Nucl. Phys.*, B32:221, 1971.
- [14] R.G. Arnold, B.T. Chertok, E.B. Dally, A. Grigorian, C.L. Jordan, W.P. Schuetz, R. Zdarko, F. Martin, and B.A. Mecking. *Phys. Rev. Lett.*, 35:776, 1975.
- [15] G.G. Simon, Ch. Schmitt, and V.H. Walther. *Nucl.Phys. A*, 364:285, 1981.

- [16] R. Cramer, M. Renkhoff, J. Drees, U. Ecker, D. Jagoda, K. Koseck, G.-R. Pingel, B. Remensnitter, A. Ritterskamp, B. Boden, V. Burkert, G. Knop, M. Leenen, R. Sauerwein, and D. Schablitzy. *Z. Phys. C*, 29:513, 1985.
- [17] S. Platchkov, A. Amroun, S. Auffret, J.M. Cavedon, P. Dreux, J. Duclos, B. Frois, D. Goutte, H. Hachemi, J. Martino, X.H. Phan, and I. Sick. *Nucl. Phys.*, A510:740, 1990.
- [18] P. Sauer and R. Henning. *Few Body Syst.*, 7:92, 1992.
- [19] H. Henning. *priv.com.*, 1997.
- [20] J.W. van Orden, N. Devine, and F. Gross. *Phys. Rev. Lett.*, 75:4369, 1995.
- [21] R. Schiavilla and D.O. Riska. *Phys. Rev.*, C43:437, 1991.
- [22] E. Hummel and J.A. Tjon. *Phys. Rev.*, C42:423, 1990.
- [23] P.L. Chung, F. Coester, B.D. Keister, and W.N. Polyzou. *Phys. Rev. C*, 37:2000, 1988.
- [24] A. Buchman, Y. Yamauchi, and A. Faessler. *Nucl. Phys.*, A468:621, 1989.
- [25] E. M. Nyman and D.O. Riska. *Nucl. Phys. A*, 468:473, 1987.
- [26] C.E. Carlson. *Nucl. Phys.*, A508:481c, 1991.
- [27] M. Garcon, J. Arvieux, D.H. Beck, E.J. Beise, A. Boudard, E.B. Cairns, J.M. Cameron, G.W. Dodson, K.A. Dow, M. Farkhondeh adn H.W. Fielding, J.B. Flanz, R. Goloskie, S. Hoibraten, J. Jourdan, S. Kowalski, C. Lapointe, W.J. McDonald, B. Ni, L.D. Pham, R.P. Redwine, N.L. Rodning, G. Roy, M.E. Schulze, P.A. Souder, J. Soukup, I. The, W.E. Turchinetz, C.F. Williamson, K.E. Wilson, S.A. Wood, and W. Ziegler. *Phys. Rev. C*, 49:2516, 1994.
- [28] P. Gueye and C. Yan. *Beam Position Monitors in Hall C. JLAB int. report.*, 1997.
- [29] C. Yan. *Nucl. Inst. and Meth. A*, 365:261, 1995.
- [30] B. Mertin. *Das Hochfrequenz-Strahlmonitorsystem fuer die 15MeV-Stufe des MAMI-Projektes*. Diplomarbeit. Johannes Gutenberg Universitaet, Mainz, 1980.

- [31] D. Mittwich. *Entwicklung und Erprobung eines Hochfrequenzmonitors zur Messung der Intensitaet und der Lage eines 855MeV Elektronenstrahls*. Diplomarbeit. Johannes Gutenberg Universitaet, Mainz, 1992.
- [32] C. S. Armstrong. *Electroproduction of the  $S_{11}$  Resonance at High Momentum Transfer*. PhD thesis, College of William and Mary, VA, 1998.
- [33] K. Unser. *IEEE Trans. Nucl. Sci.*, 16:934, 1969.
- [34] K. Unser. *IEEE Trans. Nucl. Sci.*, 28:2344, 1981.
- [35] C. Bochna. *priv. comm.*, 1996.
- [36] J. R. Arrington. *Inclusive Elastic Scattering From Nuclei at  $x>1$  and High  $Q^2$* . PhD thesis, California Institute of Technology, 1998.
- [37] D. Dutta. *The  $(e, e'p)$  Reaction Mechanism in Quasi-Elastic Region*. PhD thesis, Evanston, Illinois, 1999.
- [38] R. Ent. *priv. comm.*, 1999.
- [39] J. Mitchell. *Specifications for the control system of the hall c cryogenic targets*. *JLAB int. report.*, 1995.
- [40] J. Dunne. *Memorandum, survey of the cryotarget for t20*. *JLAB int. report.*, 1997.
- [41] K. Gustaffson. *Cryotarget Density Dependence on Beam Current*. *JLAB int. report.*, 1997.
- [42] H. Thomas. *priv. comm.*, 1999.
- [43] D. Meekins. *Coherent  $\pi^0$  Photoproduction on the Deuteron*. PhD thesis, JLab, 1998.
- [44] V. Vrolov. *Electroproduction of the  $\Delta(1232)$  Resonance at High Momentum Transfer*. PhD thesis, Rensselaer Polytechnic Institute, Troy, NY, 1998.
- [45] R. Ent. *priv. comm.*, 1998.
- [46] C. Yan. *Preliminary Users Manual of the HMS at JLab*. *JLAB int. report.*, 1997.
- [47] J. E. Ducret and M. Garcon. *CEBAF  $t_{20}$  experiment: Report on the deuteron channel*. DAPNIA/SPhN, CEA-Saclay, 1995.

- [48] S. Wood. *CEBAF Online Data Acquisition System Users Manual. JLAB int. report.*, 1994.
- [49] D. W. Perkins. *High Energy Physics*. Addison-Wesley Publ. Company, Inc., Bonn, 1990.
- [50] W. E. Burchman and M. Jobes. *Nuclear and Particle Physics*. John Wiley & Sons Inc., 605 Third Avenue, New York, 1994.
- [51] M.J. Niculescu. *Inclusive Resonance Electroproduction Data from Hydrogen and Deuterium and Studies of Quark-Hadron Duality*. PhD thesis, Hampton University, VA, USA, 1999.
- [52] M. Katz and S. Wood. *A Rewrite of the Hall C Event Display at the Thomas Jefferson National Accelerator Facility. JLAB int. report.*, 1999.
- [53] L.W. Mo and Y.S. Tsai. *Rev. Mod. Phys.*, 46:815, 1969.
- [54] S. Stein, W.B. Atwood, E.D. Bloom, R.L.A. Cottrell, H. DeStaebler, C.L. Jordan, h.G.Piel, C.Y. Prescott, R. Siemann, and R.E. Taylor. *Phys. Rev. D*, 12:1884, 1975.
- [55] Y.S. Tsai. *SLAC Report*, SLAC-PUB-848, 1971.
- [56] E. Borie. *Lettere al Nuovo Cimento*, 1.3:106, 1971.
- [57] E. Borie and D. Drechsel. *Nucl. Phys.*, A167:369, 1971.
- [58] T.W. Donnelly and Ingo Sick. *Review of Modern Physics*, 56:461, 1984.
- [59] I. The, J. Arvieux, D.H. Beck, E.J. Beise, A. Boudard, E.B. Cairns, J.M. Cameron, G.W. Dodson, K.A. Dow, M.Farkhondeh, H.W. Fielding, J.B. Flanz, M. Garcon, R. Goloskie, S. Hoibraten, J. Jourdan, S. Kowalski, C. Lapointe, W.J. McDonald, B. Ni, L.D. Pham, R.P. Redwine, N.L. Rodning, G. Roy, M.E. Schulze, P.A. Souder J. Soukup, W.E. Turchinetz, C.F. Williamson, K.E. Wilson, S.A. Wood, and W. Ziegler. *Phys.Rev.Lett.*, 67:173, 1991.
- [60] P. Vernin. *priv. comm.*, 1992.
- [61] K.Hencken, G. F. Bertsch and H. Esbensen. *Phys. Rev.*, C54:3043, 1996.
- [62] W. Bauhoff. *Atomic Data and Nuclear Data Tables*, 35, 429-447, 1986.
- [63] H.P. Wellisch and D. Axen. *Phys. Rev.*, C54/3:1329, 1996.

- [64] J.C. Peng, R.M. DeVries, and N.J. DiGiacomo. *Physics Letters*, 98B:244, 1981.
- [65] H. Anklin, L.J. deBever, K.I. Blomqvist, W.U. Boeglin, R. Böhm, M. Distler, R. Edelhoff, J. Friedrich, D. Fritschi, R. Geiges, J. Götz, A. Honegger, P. Jennewein, J. Jourdan, M. Kahrau, M. Korn, H. Kramer, K.W. Krygier, G. Kubon, V. Kunde, A. Liesenfeld, G. Masson, K. Merle, R. Neuhausen, E.A.J.M. Offermann, Th. Petitjean, Th. Pospischil, M. Potokar, L.M. Qin, A.W. Richter, R. Rokavec, G. Rosner, P. Sauer, S. Schardt, I. Sick, S. Sirca, Ph. Trueb, M. Tuccillo, B. Vodenik, A. Wagner, Th. Walcher, G. Warren, S. Wolf, J. Zhao, M. Zeier, and B. Zihlmann. *Phys. Lett. B*, 428:248, 1998.
- [66] L.C. Alexa et al. *Phys. Rev. Lett.*, 82:1374–1378, 1999.
- [67] K.R. McCormick. *Measurement of the Deuteron Elastic Structure Functions at Large Momentum Transfers*. PhD thesis, Old Dominion University, VA, USA, 1999.
- [68] H. Hacene. *These, Univ. Paris Sud*, 1986.
- [69] S. Auffret. *These, Université Paris-Sud, Orsay*, 1985.
- [70] M. Bernheim et al. *Phys. Rev. Lett.*, 46:402, 1981.
- [71] I. Sick. *Nucl. Phys.*, A218:509, 1974.
- [72] I. Sick and D. Trautmann. *Nucl. Phys. A*, 637:559, 1998.
- [73] M. Lacombe, B. Loiseau, R. Vinh Mau, J. Cote, P. Pires, and R. de Tourreil. *Phys. Lett.*, 101B:139, 1981.
- [74] R. Machleidt, K. Holinde, and Ch. Elstert. *Phys. Rep.*, 149:1 and 373, 1987.
- [75] R.B. Wiringa. *priv. comm.*, 1994.
- [76] E. Hummel and J.A. Tjon. *Phys. Rev. C*, 49:21, 1994.
- [77] J.W. Van Orden, N. Devine, and F. Gross. *Phys. Rev. Lett.*, 75:4369, 1995.
- [78] H. Ito and F. Gross. *Phys. Rev. Lett.*, 71, 1993.
- [79] D.R. Phillips, S.J. Wallace, and N.K. Devine. *Los Alamos preprint*, nucl-th/9802067, 1998.

- [80] D.R. Phillips and T.D. Cohen. *Los Alamos preprint*, nucl-th9906091, 1999.
- [81] P. Mergell, U.-G. Meissner, and D. Drechsel. *Nucl. Phys.*, A596:367, 1996.
- [82] R. Serber. *Phys. Rev.*, 72:1008, 1947.
- [83] R. J. Glauber. *Phys. Rev.*, 99:1515, 1955.
- [84] C. A. Bertulani and K. W. McVoy. *Phys. Rev.*, C46:2638, 1992.
- [85] D. Pitz. *Precise Measurement of the Deuteron Elastic Form Factor A(Q<sup>2</sup>)*. PhD thesis, SACLAY, 1999.
- [86] S. K. Charagi and S. K. Gupta. *Phys. Rev.*, C41:1610, 1990.
- [87] L. Ray. *Phys. Rev.*, C20:1857, 1979.
- [88] H. de Vries, C.W. de Jager, and C. de Vries. *Nuclear and Atomic Data Tables*, 36:495, 1987.
- [89] I. Sick. *priv. comm.*, 1999.
- [90] J. S. Al-Khalili, J. A. Tostevin, and I. J. Thompson. *Phys. Rev.*, 54:1843, 1996.

## Lebenslauf

Die Primarschule besuchte ich in Reinach (BL). Es folgten zwei Jahre Progymnasium in Aesch (BL) sowie ein weiteres Jahr Mittelstufe an der Bezirksschule Breitenbach (SO). Nach vier Jahren am Gymnasium in Laufen (BL) schloss ich im Herbst 1989 mit der Matura Typus C ab.

Im November 1990 begann ich an der ETH Zürich mit dem Studium der Ingenieurwissenschaften, von welchem ich im folgenden Frühjahr direkt ins Sommersemester des ersten Jahreskurses Physik der Uni Basel (Nebenfach Bio II) wechselte, um im Frühjahr 1995 abzuschliessen.

Nach einem sechsmonatigen Master of Science Kursus in Strahlenbiologie am St. Bartholomew's Hospital in London (1995) folgte ab März 1996 unter der Leitung von Prof.Dr. I. Sick und PD.Dr. J. Jourdan die Teilnahme an diversen Streuexperimenten am Hadronenbeschleuniger Paul-Scherrer-Institut (PSI) sowie den Elektronenbeschleunigern Mainzer Mikrotron (MAMI) und Jefferson Accelerator Facility (TJNAF).

Während meiner Dissertation war ich unter den Herren Prof. Dr. P. Oelhafen und Prof. Dr. E. Meyer als Vorlesungsassistent in der Vorlesung für Studierende der Medizin und Pharmazie tätig.

Seit dem 1. August 1998 bin ich mit Nicole Honegger-Feigenwinter verheiratet. Zu Weihnachten erwarten wir Nachwuchs!

Meine Ausbildung in den Fächern Experimentalphysik, theoetische Physik, Mathematik, Informatik, Pädagogik & Didaktik sowie Bio II verdanke ich folgenden Dozentinnen und Dozenten:

N. A'Campo, C. Bandle, G. Backenstoss, G. Baur, H. Burckhardt, P. Diehl, O. Dörfler, J. Engel, F.J. Elmer, R. Franklin, J. Fünfschilling, H.J. Güntherodt, H.P. Hauri, H.Ch. Im Hof, J. Jourdan, K. Kirschner, H. Kraft, H. Kubli, J.G. Nicholls, P. Oelhafen, H. Rudin, G. Schatz, I. Sick, L. Tauscher, H. Thomas, D. Trautmann, Ch. Ullrich, D. Vossiek, R. Wagner, I. Zschokke-Gränacher.